

# Mechanisms of the Overturning Circulation in the Northern Red Sea, more than Convective Mixing

Lina Eyouni<sup>1,2</sup>, Zoi Kokkini<sup>1,3</sup>, Nikolaos D. Zarokanellos<sup>1,4</sup>, Burton H. Jones<sup>1</sup>

<sup>1</sup> King Abdullah University of Science and Technology (KAUST), Biological and Environmental Sciences and Engineering (BESE), Red Sea Research Center (RSRC), Thuwal, Saudi Arabia.

<sup>2</sup> Red Sea Global (RSG), Riyadh, Saudi Arabia.

<sup>3</sup> Consiglio Nazionale Delle Ricerche (CNR), Istituto di Scienze Marine (ISMAR), Lerici, Italy

<sup>4</sup> Balearic Islands Coastal Observing and Forecasting System (SOCIB), Palma de Mallorca, Spain

*Correspondence to:* Zoi Kokkini ([zoi.kokkini@sp.ismar.cnr.it](mailto:zoi.kokkini@sp.ismar.cnr.it))

**Abstract.** The northern Red Sea (NRS) is where Red Sea Outflow Water (RSOW) and, occasionally, Red Sea Deep Water are formed. Glider observations are used to describe the formation mechanisms and pathways of the intermediate waters in the NRS in late winter from 31 January to 18 April 2019. Utilizing glider observations, atmospheric reanalysis products, and satellite datasets, we evaluated the mesoscale activity and the atmospheric conditions that contribute to outflow water formation. The cyclonic circulation in the region surfaces dense water, which exposes it to the atmosphere, ventilating the water column and contributing to phytoplankton growth (enhancement of chlorophyll concentration) due to the nutrients upwelled into the euphotic layer (Zeu). Subduction of this water in the 3-dimensional cyclonic circulation transported oxygenated, elevated chlorophyll water to depths between 150 m and 250 m along the 28.2 kg/m<sup>3</sup> isopycnal. Unlike previous observations, in late February, a strong anticyclonic circulation blocked the inflow of warmer, fresher water into the region. It was accompanied by a negative heat flux and an uplifting of dense water to the surface. Net cooling through mid-March cooled the incoming surface waters from the south. At the end of the observational period, the intrusion of warmer, fresher waters from the south coincided with the re-establishment of cyclonic circulation and capped the dense surface water that had formed during March. These observations demonstrate that multiple processes

- 28 contribute to RSOW formation: convective mixing, cyclonic uplifting of dense water, subduction, and
- 29 meso- (submeso-) scale processes.

## 1. Introduction

The Red Sea (RS) is a narrow, elongated, meridionally oriented basin lying between the Asian and African continents. Its subtropical location results in significant buoyancy losses due to high evaporation (nearly 2 m/yr), negligible precipitation, and effectively no riverine inputs, resulting in it being one of the world's saltiest and warmest seas (Edwards and Head, 1987; Smeed, 1997; 2004; Sofianos et al., 2002). The RS experiences seasonally reversing winds over the southern region, coupled with the Arabian Sea's monsoonal forcing. The reversing winds control the circulation and water mass exchange through the Strait of Bab al Mandab (Abualnaja et al., 2015; Patzert, 1974). These processes, along with the buoyancy forcing, drive the large-scale circulation (Bower and Farrar, 2015; Murray and Johns, 1997; Patzert, 1974; Sofianos and Johns, 2007). The inflow of water from the Gulf of Aden compensates for the evaporative water loss in the RS. The advected northward waters contribute to the overall latitudinal gradient in salinity and temperature from the south to the north. The northward advection of comparatively fresh and warm water from the south has an important role in the stratification (Asfahani et al., 2020; Churchill et al., 2014; Sofianos and Johns, 2007; Zarokanellos et al., 2017b), with the annual flux into the RS reaching up to 0.22 Sv (Sofianos and Johns, 2002). This water has been traced to the NRS at 28°N (Zarokanellos et al., 2017a). It is modified through heating, evaporation, and mixing as it progresses northward (Cember, 1988; Sofianos and Johns, 2003; Sofianos and Johns, 2007).

Significant mesoscale activity is found along the RS's main axis (Morcos, 1970; Morcos and Soliman, 1972; Quadfasel and Baudner, 1993; Sofianos and Johns, 2007; Zhan et al., 2014) that results from baroclinic instabilities (Zhan et al., 2014) and the presence of the Eastern Boundary Current (EBC; Zarokanellos et al., 2017a, 2017b; Biton et al., 2010; Biton et al., 2008; Bower and Farrar, 2015; Eshel et al., 1994; Eshel and Naik, 1997; Sofianos and Johns, 2007). Some of these mesoscale eddies are thought to be quasi-permanent features, in particular the cyclonic eddy (CE) in the Northern Red Sea (NRS) and the anticyclonic eddy (AE) in the Central Red Sea (CRS) (Chen et al., 2014; Yao et al., 2014b). The CE in the NRS plays a crucial role in forming the RSOW (Asfahani et al., 2020; Sofianos and Johns, 2007). Zarokanellos et al. (2017a) have shown that an AE in the CRS can redirect or deflect the advected northward flow of Gulf of Aden water. These mesoscale eddies substantially affect heat and salt advection and distribution of biogeochemical properties (Chen et al., 2014; Raitzos et al., 2013; Triantafyllou et al.,

2014), which are often useful tracers of physical processes. Eddies also transfer energy and momentum to the mean flow, driving the circulation (Lozier, 1997). In addition, mesoscale features fundamentally modulate local nutrient fluxes and phytoplankton dynamics (Longhurst, 2007). Eddy activity in the RS has shown that it significantly influences the optical and biological properties (Kürten et al., 2016; Mahadevan, 2015; McGillicuddy et al., 1998; Pearman et al., 2017; Siegel et al., 2008). In particular, mesoscale eddies in the RS facilitate the vertical transport of nutrients into the upper water column, thereby impacting biogeochemical variability (Zarokanellos et al., 2017; Kürten et al., 2019).

Mesoscale processes can induce subduction events over larger areas with significant impact in the marine ecosystem (Mahadavan et al. 2016). Subduction is the process where physical and biogeochemical tracers transport from the surface to the interior. This, in turn, influences the chlorophyll flux in the Zeu playing a significant role in the RS biological variability. Furthermore, while the upper ocean is primarily ventilated through subduction events, the ventilation in the deep ocean occurs primarily through open-ocean convection (Asfahani et al., 2020; Williams and Meijers 2019). Seasonal mixing, eddy interactions, and cross-shelf exchange drive biogeochemical fluxes in the upper layer. In the RS, seasonal phytoplankton variability has been studied primarily through remote sensing (Acker et al., 2008; Gittings et al., 2018; Racault et al., 2015; Raitzos et al., 2013), with only a few studies incorporating in situ observations (Kheireddine, 2020; Zarokanellos et al., 2017a, 2017b; Zarokanellos & Jones, 2021). These studies highlight ecological connections between coastal and open-sea regions, vital for coral communities (Acker et al., 2008; Raitzos et al., 2017). However, remote sensing is limited to surface observations, as ocean color data do not capture subsurface phytoplankton distributions. Integrating bio-optical data from both remote sensing and in situ measurements has provided valuable insights into the RS's biogeochemical dynamics (Brewin et al., 2015; Gittings et al., 2018; Kheireddine et al., 2020; Racault et al., 2015; Raitzos et al., 2013; Tiwari et al., 2018; Zarokanellos et al., 2017a, 2017b; Zarokanellos & Jones, 2021).

Water mass transformation typically occurs in the surface ocean in specific regions where air-sea interaction acts powerfully on the upper layer (Emery, 2001; Iselin, 1939). Significant surface cooling results in buoyancy loss that can contribute to deep mixing and convection. The NRS has been considered the main area of RSOW formation and, occasionally, Red Sea Deep Water (RSDW) formation

86 (Papadopoulos et al., 2015; Sofianos and Johns, 2003; Sofianos and Johns, 2007; Yao et al., 2014 b), due  
87 to the high evaporation rates and significant surface water cooling that occur during winter (Papadopoulos  
88 et al., 2013). These preconditions, in addition to the presence of the CE, where shallowing of the  
89 isopycnals occurs at the eddy center, contribute to the formation of the aforementioned RSOW and RSDW  
90 (Abualnaja et al., 2015; Asfahani et al., 2020; Sofianos and Johns, 2003; Yao et al., 2014 b; Zhai et al.,  
91 2015). The newly formed RSOW gradually sinks until it reaches an equilibrium density of near 27.5 to  
92 27.7 kg/m<sup>3</sup> throughout the basin (Zhai et al., 2015) and flows southward, where it exits the RS through  
93 the strait of Bab-El-Mandeb (Cember, 1988; Sofianos and Johns, 2003; Yao et al., 2014 b). Once it enters  
94 the Gulf of Aden, it is mixed due to the intense mesoscale eddy activity at depths between 400 and 1000  
95 m (Bower and Furey, 2010). Despite significant dilution of the thermohaline properties, RSOW has been  
96 observed as far southward as the Agulhas Current below 32°S (Beal et al., 2000) and as far east as the  
97 Bay of Bengal (Jain et al., 2017).

98 Numerical simulations and a few in-situ observations suggest three potential mechanisms for RSOW  
99 formation. The first mechanism, open-ocean convection, is associated with the presence of a cyclonic  
100 gyre in the NRS (Sofianos and Johns, 2007; Papadopoulos et al., 2015). Strong atmospheric forcing in  
101 the region and the presence of cyclonic gyre creates favourable conditions for convection events. The  
102 second mechanism is mixed layer deepening during winter, resulting from a large negative heat flux (Zhai  
103 et al., 2015). The third mechanism is the combined effect of the cyclonic gyre and the weakening of the  
104 stratification that results from strong atmospheric forcing (Chen et al., 2014; Clifford et al., 1997;  
105 Manasrah et al., 2004; Morcos and Soliman, 1972; Yao et al., 2014 b). Concurrent with the formation of  
106 the RSOW, the RSDW forms in the NRS when strong cooling and evaporation occur in the gulfs of Suez  
107 and Aqaba (Cember, 1988; Papadopoulos et al., 2015; Sofianos and Johns, 2003; Yao et al., 2014 b). The  
108 RSDW is evident below 300 m, while the RSOW is typically found between 200 and 300 m and can be  
109 identified by the relatively high oxygen concentration, which can be distinguished from the RSDW. The  
110 regionally formed RSOW has a significant role in the overturning circulation, as indicated by in-situ  
111 observations and numerical simulations (Papadopoulos et al., 2015; Sofianos and Johns, 2003; Zhai et al.,  
112 2015). In addition, RSOW contributes to the ventilation of the RS (Papadopoulos et al., 2015; Sofianos

113 and Johns, 2007; Woelk and Quadfasel, 1996; Yao et al., 2014 b; Zhai et al., 2015) and the salt budget of  
114 the Indian Ocean due to the high salinity concentrations present in intermediate depths (Beal et al., 2000).  
115 The primary objective of this study is to understand the mechanisms that contribute to the mass  
116 formation of RSOW in the NRS and the biogeochemical responses associated with these physical  
117 processes. The second objective is to evaluate how atmospheric forcing affects mesoscale dynamics in  
118 the study area. This paper is organized as follows: In Section 2, the in-situ, reanalysis, and remote sensing  
119 observations are presented. Section 3 describes the coupling of the atmospheric forcing and the in-situ  
120 observations. A comprehensive description of the flow variability and the mechanism of RSOW  
121 formation is described, including the coupling between physical and biogeochemical processes in the  
122 study area. Finally, Section 4 presents a discussion and comparison with previous regional studies, along  
123 with the conclusions.

124

125       **2. Data and methods**

126       **2.1 Glider observations**

127       A sustained glider line that was traversed in a 3–4-day period in the NRS was used to capture the  
128 wintertime evolution of physical and biogeochemical characteristics in the NRS (Eyouni et al., 2024).  
129 The Seaglidors (hereinafter “gliders”) were equipped with a CTD, a dissolved oxygen sensor, and a triplet  
130 fluorometer (**Table 1**). The glider was deployed along a transect oriented approximately perpendicular to  
131 the coastline offshore from Duba, referred to as the “Duba line” (**Fig. 1a**). The line extended from  
132 approximately 5 km off the coast to nearly 75 km offshore. The glider completed each transect in about  
133 3.5 days and was programmed to dive from the surface to ~750 m. The average horizontal speed was ~25  
134 cm/s, and each dive cycle took ~3 hours to complete, depending on the target depth, topography, and sea  
135 conditions. The deployment spanned the period from 31 January to 21 April, 2019 (**Table 1, Fig. 1b**).  
136

Deployment Location	Observation Period	Duration (days)	Sensors	Parameter
NRS	30.01.2 019/22.04.2 019	83	Seabird, unpumped CT	CTD (Conductivity, Temperature, Pressure)
			WETlabs EcoPuck Fluorometer (FL3-IRB sensor)	Chlorophyll Fluorescence (CHL), Colored Dissolved Organic Matter (CDOM), Phycocyanin
			WETlab Backscatter (BB3 IRB sensor)	Backscatter at 532, 650, and 880 nm
			Aanderaa Optode (4330)	Dissolved Oxygen (DO)

138     **Table 1:** Summary of the measured variables and their corresponding sensors deployed on the glider.



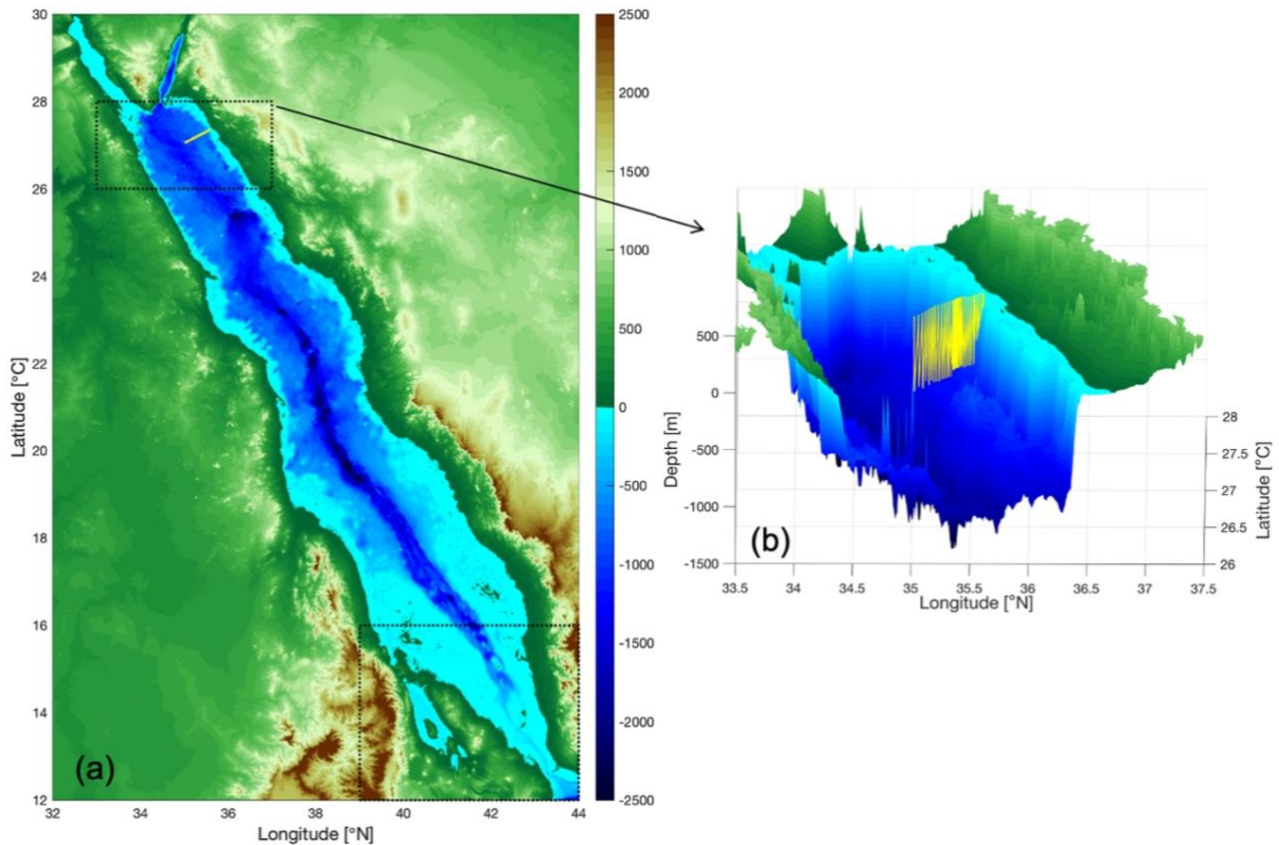


**Fig. 1:** Topographic map of the RS. The two black dash boxes in the northern and southern RS show the study area in the north and the region in the south where exchange with the Gulf of Aden occurs. The yellow line inside the northern box indicates the glider line location, and b) the yellow sawtooth line represents the undulating trajectory of the glider superimposed on the bathymetry, which has been reproduced from the GEBCO\_2021 Grid, GEBCO Compilation Group (2021; <https://doi.org/10.5285/c6612cbe-50b3-0cff-e053-6c86abc09f8f>).

Each vertical profile has been examined for spikes and outliers before further analysis. No evidence of thermal lag has been observed in the CT observations. The WETlabs EcoPuck Triplet Fluorometer (FL3) and backscatter (BB3) sensor were factory calibrated, and dark counts were measured prior to

deployment to account for any drift. However, the BB3 sensor starts to drift on 26 March 2019. The pre-deployment dark counts for the FL3 were consistent with factory dark counts. Roesler et al. (2017) performed a global comparison of fluorometer and extracted CHL measurements and recommended that factory-calibrated chlorophyll should be divided by two. Thus, CHL here is divided by 2 to correspond to in situ CHL concentrations as described in Roesler et al. (2017). As the RS is a region with high irradiance, the CHL can often experience quenching. In this study, we examined the vertical profiles of CHL fluorescence for quenching, and no significant quenching was detected. The oxygen measurements were adjusted by a correction factor based on the median oxygen saturation in the upper 10 m. The correction factor was the ratio of the median oxygen saturation concentration for the upper 10 m to the median measured concentration within the upper 10 m of the water column. The entire water column data was then corrected by multiplying the reported oxygen concentrations by the correction factor. The correction provided consistency between the current glider data set and the vertical distribution for this region in the World Ocean Atlas (Zarokanellos and Jones, 2021; Garcia et al., 2019a). To facilitate data processing, plotting, and analysis, the corrected data were projected onto a grid with a vertical resolution of 2 m and a horizontal resolution of 2.5 km, the nominal distance between glider surfacing during the mission. This study focuses on the upper 500 m of the water column. Mixed Layer Depth (MLD) was calculated for each vertical profile based on a density difference of  $\leq 0.03$  kg/m<sup>3</sup> relative to the density at 10 m depth (de Boyer Montégut et al., 2004). The Brunt-Vaisala frequency (BVF) was computed to measure stratification. Geostrophic velocity and potential density were also calculated using the TEOS-10 toolbox (TEOS, SCOR, and IAPSO, 2010). The level of no motion in the geostrophic velocity has been examined, and no significant motion below 500 m has been observed.

172

## 173       **2.2 Remotely sensed data**

### 174       **2.2.1 Sea Level Anomaly (SLA)**

175       Previous satellite observations and numerical simulation studies suggest a cyclonic gyre located in  
176 the NRS concurrent with convective mixing where the RSOW water mass is formed (Sofianos and Johns,  
177 2002; Zhai et al., 2015). Therefore, in this study, SLA data were used to characterize the spatial and  
178 temporal evolution of the large-scale circulation patterns of sea level and geostrophic velocity during the

wintertime. The SLA data is based on the multi-mission altimeter Archiving Validation and Interpretation of Satellite Oceanographic Data (AVISO) provided by the Copernicus Marine Environment Monitoring Service (CMEMS). The data has been gridded at a regular  $0.258^\circ \times 0.258^\circ$ . The obtained daily measured data were taken within the domain from  $20^\circ$  to  $28^\circ$  N and  $32^\circ$  to  $42^\circ$  E, inclusive of the glider deployments. Within the NRS subdomain ( $26 - 28^\circ$  N,  $33 - 37^\circ$  E), the data were temporally averaged to fit approximate the periods of the glider transects. Previous work has validated the use of the AVISO product from comparisons with both in situ and numerical model results (Hernandez and Schaeffer, 2001; Zhan et al., 2014; Zarokanellos et al., 2017).

### 2.2.2 Sea Surface Temperature (SST)

Sea surface temperature (SST) data were obtained from the Moderate Resolution Imaging Spectroradiometer (MODIS) imagery that provides a daily image with a spatial resolution of 4 km. The data were obtained within the domain from  $24^\circ$  to  $28^\circ$  N to identify and determine the spatial and temporal evolution of the large-scale patterns of the SST (Werdell et al., 2013).

## 2.3 Atmospheric reanalysis products

Atmospheric parameters for this study were derived from the Modern-Era Retrospective Analysis for Research and Applications Version 2 (MERRA-2) reanalysis dataset (Rienecker et al., 2011; Gelaro et al., 2017). MERRA-2 offers a high-resolution representation of atmospheric conditions, providing daily mean values on a  $0.5^\circ \times 0.652^\circ$  grid with a temporal resolution of one hour. This dataset was chosen due to its demonstrated accuracy in representing heat fluxes within the region of interest, as validated by recent studies such as Al Senafi et al. (2019). For this analysis, data were extracted and spatially averaged over a defined box encompassing the NRS ( $26 - 28^\circ$  N,  $33 - 37^\circ$  E; **Fig. 1a**), excluding land coverage. Daily means were calculated from the hourly data for the selected parameters of wind speed and direction, surface net heat flux ( $Q_{net}$ ), and evaporative heat flux, which is considered to be the primary driver of heat loss in the RS (Sofianos and Johns, 2003).

The  $Q_{net}$ , produced using the Coupled Ocean-Atmosphere Response Experiment (COARE 3.0) formulation (Fairall et al., 1996), consists of the sum of shortwave ( $Q_{sw}$ , absorbed), longwave ( $Q_{lw}$ , emitted), latent ( $Q_L$ , evaporative), and sensible ( $Q_s$ , conductive) heat fluxes, as all terms are positive when they are heating the water column. The quantity  $Q_{net}$  is calculated using the following formula:

$$Q_{net} = Q_{sw} + Q_{lw} + Q_s + Q_L \quad (1)$$

## 2.4 Empirical Orthogonal Function (EOF) analysis

To compare the SLA from 2019 with observations from the preceding years, EOF analysis is carried out on SLA data to evaluate the spatial and temporal patterns of the variability of the SLA data in the winter-spring period. Each eigenvector describes the spatial pattern (modes) of that variability for five months from January to May for the years 2016, 2017, 2018, and 2019. Only the first mode of the EOF is used to compare the seasonal evolution of the spatial pattern each year. In addition, the explained variance with the eigenvalue provides the relative contribution that a specific mode contributes to the variability (Zhang and Moore, 2015).

## 2.5 One-dimensional mixed layer model

Price-Weller-Pinkel (PWP) mixed layer model (Price et al., 1986) has been applied to evaluate the local atmospheric effects on the ocean mixed layer. The model input includes the following terms: radiative heat flux (shortwave, longwave), latent and sensible heat, freshwater flux (evaporation [E] and precipitation [P];  $[E - P]$ ), and wind stress components  $[\tau_x \text{ and } \tau_y]$ . As the RS is sandwiched between two extreme desert regions, precipitation is considered to be negligible ( $P=0$ ). The 1-D PWP has been applied to estimate the local, atmospherically-driven evolution of the mixed layer depth during the observation period. The model was executed for three sequential subsets delineated from the glider observations: the cooling phase, the cool, salty, dense phase, and the warming-freshening phase. The model was initialized with the average temperature and salinity profile for one complete glider transect at the beginning of each simulation period (30 days) and then stepped forward in 24-hour (1-day)

increments subject to the heat, freshwater, and momentum fluxes. The daily time step was selected as insignificant diurnal variability was observed in mixed layer temperature and salinity from the glider.

The PWP model produces a mixed layer through a vertical exchange process between the air and sea interaction and vertical mixing. It assimilates time series of surface heat flux, wind, and precipitation and applies these forcing parameters to the initial vertical profile of temperature and salinity. The model interpolates the momentum components driven by winds, cooling, and evaporation to induce convective instability, entrainment from the pycnocline, and a mixing term generated from vertical current shear. In our case, since  $P=0$ , only surface heating affects re-stratification.

The convective adjustment in the PWP model starts with grid cells with unstable stratification being homogeneously blended with neighbouring cells. The convective correction follows the bulk mixed layer parameterization, where the mixed layer deepens when the bulk Richardson number,  $R_{ib}$ , falls below a threshold value of 0.65 (Price et al., 1986).

The bulk Richardson number is expressed as:  $R_{ib} = \frac{\Delta \rho g}{\rho_0 (\Delta U)^2}$  (2)

where  $\Delta \rho$  (density) and  $\Delta U$  (*velocity*) are the differences between their values within the mixed layer, and their values below the mixed layer, respectively (Price et al., 1986). The variable  $\rho_0$  is the reference density and  $g$  is the gravitational acceleration. Then, the model adds local shear instability below the mixed layer, where mixing due to strong shear is parameterized based on a threshold gradient Richardson

number,  $R_{ig}$ , defined as:  $R_{ig} = \frac{N^2}{S^2} = 0.25$  (2a)

where,  $S^2$  is the square of the shear below the mixed layer and  $N^2 = \frac{g}{\rho} \frac{\Delta \rho}{\Delta z}$  (2b)

The vertical resolution of the model depth bin was set to 2 meters to be aligned with the gridded glider data. The momentum (horizontal diffusivity) and vertical diffusivity were set to  $10^{-5}$  m<sup>2</sup>/s and 0 m<sup>2</sup>/s, respectively (Sanikommu et al, 2020; Zhai et al., 2015). The maximum depth of the PWP experiment for the run and the initial depth range for the profiles of salinity and temperature were 400 m, the depth at which the divergence of hydrographic variables between summer and winter was minimal. Estimation of the MLD at each time step throughout the PWP model run used the same criteria used for the glider data by determining the depth range over which the density increase relative to 10 m was no more than 0.03 kg/m<sup>3</sup> (de Boyer et al., 2004).

### 3. Results

#### 3.1 Atmospheric forcing

Regional atmospheric forcing is a major factor affecting the seasonal variability of the RS circulation. The wind direction in the northern part of the RS is predominantly from the north-northwest (NNW; **Fig. 2a**). The net heat flux was initially negative, with heat flux losses of up to 300 w/m<sup>2</sup> in January, up to 250 w/m<sup>2</sup> in February, and transitioning in late March from net negative to net positive, thus beginning the onset of the seasonal heating period (**Fig. 2b**).

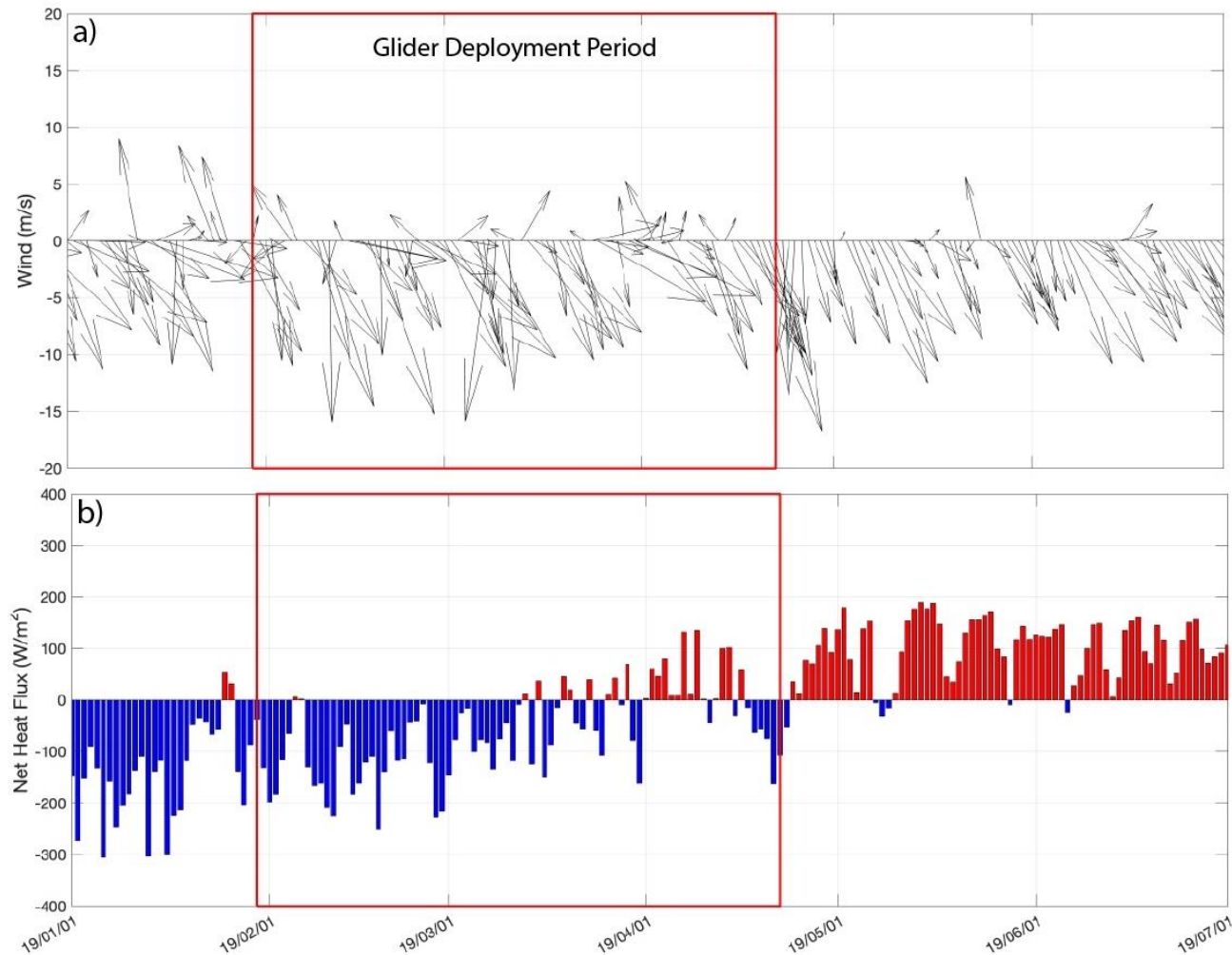


**Fig. 2:** a) Wind vectors for the NRS and b) net heat flux for the NRS (average for the black dashed box over the NRS, **Fig. 1**) for the period from January 1, 2019 through July 1, 2019. The red box indicates the period of the glider mission.

### 3.1 Upper Ocean response to atmospheric forcing

#### 3.1.1 Regional response from a remote sensing perspective

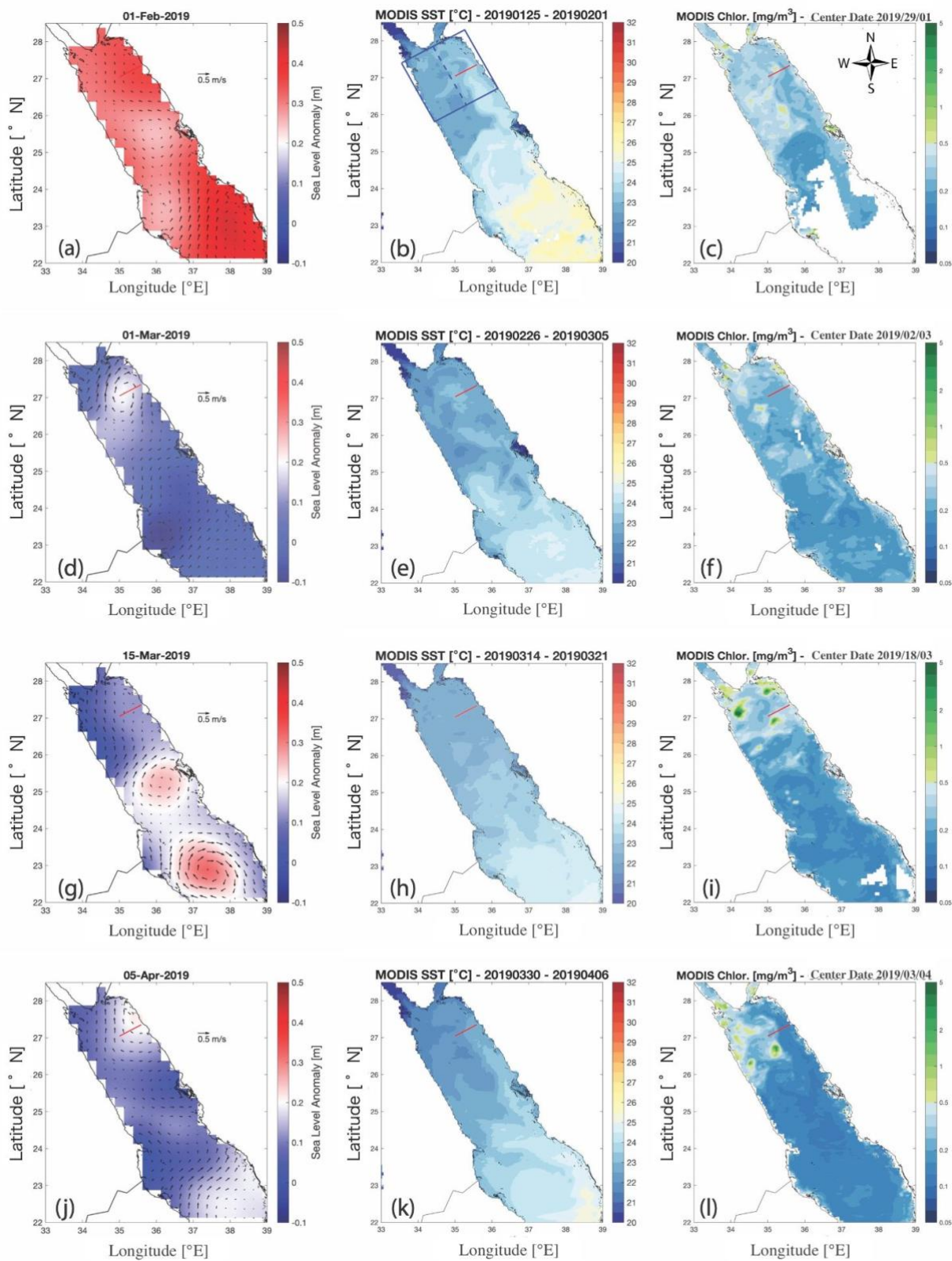
Remotely sensed ocean imagery demonstrates the seasonal evolution of the upper ocean during the glider deployment. **Fig. 3** provides images of 8-day composites for SLA and SLA-derived geostrophic velocity, sea surface temperature, and CHL concentration. At the onset of the glider deployment in late January–early February, the eastern boundary coastal flow was northward (**Fig. 3a**). Consistent with this northward flow, a tongue of warmer, low-CHL water extended northward along the Saudi coastline (**Figs. 3b–c**). These observations are consistent with previous observations from 2016 (Asfahani et al., 2020) and with the mean structure typically observed for SST in the winter months (Karnauskas and Jones, 2018). Cooler, higher CHL water is observed on the western side of the basin, perhaps due to the convective mixing described by Kheireddine et al. (2020).

Following the initial phase of northward coastal flow, an AE developed in the northeastern RS (**Fig. 3d**). During this period, the flow was southward across the glider line, and there was no indication of northward advection of warmer, low-CHL water (temperature  $> 24^{\circ}\text{C}$  and  $\text{CHL} < 0.1 \text{ mg/m}^3$ ) from the south (**Figs. 3e–f**). The AE appeared to block the warmer, low-CHL water transport into the region. The surface temperature of the NRS became cooler reaching a mean surface temperature near  $22.5^{\circ}\text{C}$  and the temperature difference between the western and eastern sides of the northern region decreased to less than  $0.25^{\circ}\text{C}$  (**Figs. 3h** and **4a**).

In the latter half of March, two anticyclonic eddies (**Fig. 3g**), between  $22^{\circ}\text{N}$  and  $26^{\circ}\text{N}$ , apparently blocked the northward flow of water from the south and isolated the northern part of the RS from the inflow of the warmer, low-CHL water. Consequently, the near-surface in the NRS became almost thermally homogeneous, with small temperature variations in its spatial distribution (**Fig. 3h**). The densest surface water was observed in the NRS during this period (**Fig. 4c**). By the beginning of April, these two eddies had dissipated, and warm, low CHL water again advected into the NRS along the eastern coastline

297   **(Figs. 3j, 3k, and 3l)**, re-establishing the temperature differential between the eastern and western halves  
298   of the NRS (**Figs. 4a-c**).





300 **Fig. 3:** 8-day averages of sea level anomaly and geostrophic velocity (left-hand panels) from AVISO as  
301 provided by the Copernicus Marine Environment Monitoring Service (CMEMS), 4 micron nighttime SST  
302 from the MODIS Aqua satellite (center panels), and CHL from MODIS OCI (right-hand panels) during  
303 the presence of the EBC (panels a-c), AE (panels d-f), pair of anticyclonic eddies (panels g-i), and lateral  
304 advection (panels j-l). The red line indicates the location of the Duba glider track. The blue box in panel  
305 b) indicates the region of the northern RS (NRS) that was used for regional averages (~ 200 km x 200  
306 km). The dashed blue line divides the eastern half of the NRS from the western half.

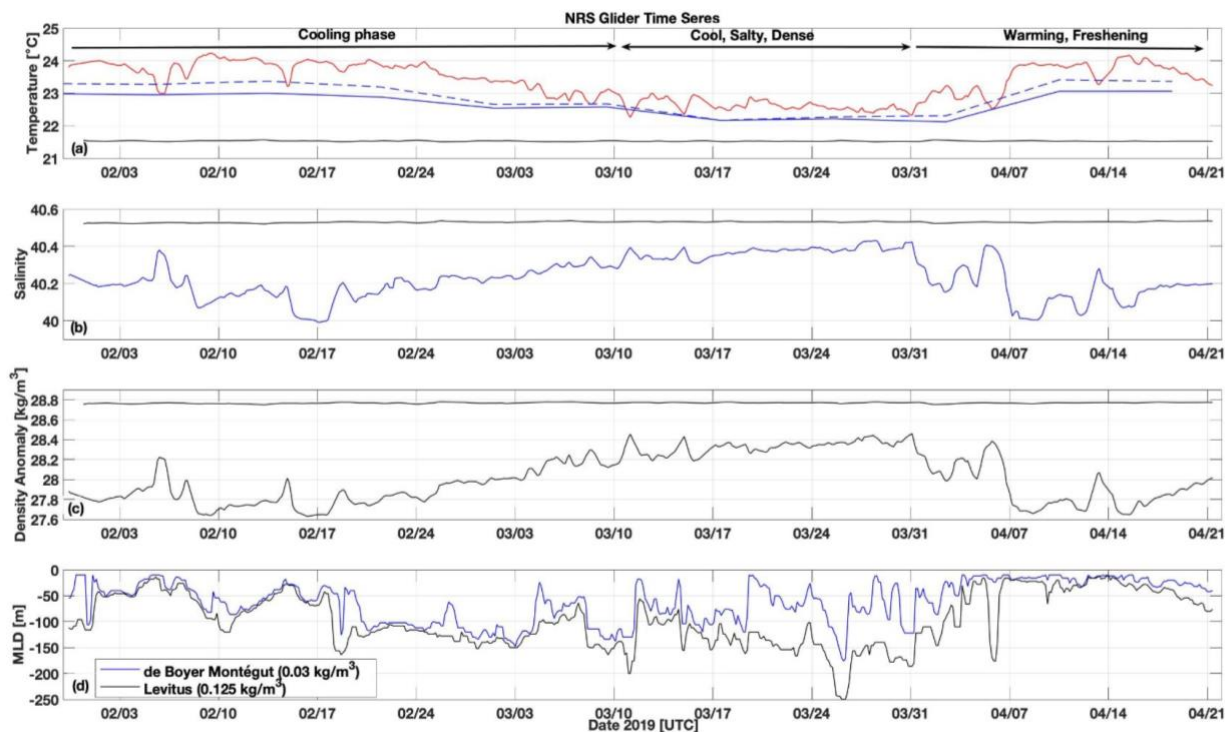
### 3.1.2 Upper layer variability

As the atmosphere progressed through its typical annual cycle, the near-surface ocean demonstrated high variability. In order to compare the data accurately, the depth of 6 m has been chosen to represent the near-surface layer, while the depth of 500 m has been selected to represent the near-bottom layer, as it is the most isolated from the surface influence and shows the least variability within the data set. The time series of surface (6 m) and 500 m values for temperature, salinity, and density are shown in **Fig. 4**. This is a continuous time series of glider data, irrespective of its location along the transect. Distinct phases are evident in the time series. The early phase, consistent with the atmospheric forcing, shows a general cooling trend from mixed layer temperatures near 24 °C in the early period to about 22.5 °C during the coolest phase, after which temperatures rose again to nearly 24 °C. For most of the period, the western half of the northern RS was cooler than the eastern half, where the glider was operating (**Fig. 4a**). However, during the coolest period, the temperatures were nearly homogeneous across the entire northern RS. Correspondingly, mixed layer salinities rose from values of 40–40.2 during the early phase to nearly 40.4 during the cool, salty period, then returned to values between 40 and 40.2 in the warming period. As a result, the near-surface density anomaly initially increased from 27.6–27.8 kg/m<sup>3</sup> to 28.3–28.4 kg/m<sup>3</sup> during the dense period. As expected, no effects of the surface forcing were apparent at 500 m.

In the latter part of the cooling phase (between February 17 and March 12), the MLD exceeded 100 m much of the time. Although the deepest mixed layer occurred during the cool, salty phase, the MLD during this period was highly variable (**Fig. 4d**). The variability in the MLD is a result of the new, well-formed cyclonic eddy during that time. Shallow MLD can be present in the center of a newly-formed cyclonic eddy, as is shown in **Fig. 7**, and it is also consistent with the patchiness of the SST (**Fig. 3e**).

Individual glider sections provide insight regarding mesoscale processes occurring in the NRS during this winter-spring period. In the early cooling phase, the isopycnals were tilted strongly downward from offshore to nearshore, with cool, dense water near the surface offshore and warmer, fresher water near the surface nearshore (**Figs. 5a** and **5b**). The overall geostrophic flow was northward, with an average velocity of 0.31 m/s in the upper 100 m (**Fig. 5e**), consistent with the geostrophic velocity calculated from the sea level anomaly (**Fig. 3a**). The maximum upper layer stratification occurred in the offshore 20 km of the transect, where uplifting of the pycnocline resulted from the cyclonic circulation (**Fig. 5d**). The

335 maximum near-surface CHL concentration occurred where dense water ( $\geq 28.1$  kg/m<sup>3</sup>) offshore  
 336 shallowed to within 50 m of the surface.



337  
 338 **Fig. 4:** Time series of near-surface (6 m) and deep (500 m) temperature, salinity, density, and MLD for  
 339 the glider deployment from January 31 through April 21, 2019. This is the complete time series,  
 340 irrespective of the glider's location along the transect. In panel a, temperature averages from the 8-day  
 341 MODIS SST are shown for the entire NRS (solid blue line), the eastern half of the northern RS (NRS-  
 342 East, dash blue line), and the western NRS (NRS-West, dotted blue line). The geographical boundaries  
 343 of these subregions are shown in **Fig. 3b**.

344 A small-scale cyclonic feature centered about 43 km offshore was embedded within the larger-scale  
 345 flow (**Figs. 5a, 5b, and 5e**). This feature was not observed in either the previous or subsequent transect,  
 346 each separated by approximately 3 days from the current transect. Thus, it was a transient feature on the  
 347 glider line, which we conclude was advected across the glider line within the larger scale flow. A feature  
 348 characterized by elevated CHL ( $\sim 30 \times 10^{-3}$  mg/m<sup>3</sup>) and DO ( $\sim 178$   $\mu$ mol/kg) was observed along the

349 28.2 isopycnal, between 20 and 40 km offshore, compared to the rest of the transect where CHL was  $\sim$   
350  $5 \times 10^{-3} \text{ mg/m}^3$  and DO  $\sim 94 \text{ } \mu\text{mol/kg}$ , respectively, while low BVF is observed in the same area. The  
351 feature spanned at a depth range from approximately 150 m at 40 km offshore to 250 m at 20 km offshore,  
352 suggestive of subduction of denser near-surface water and downward transport along the isopycnal below  
353 the mixed layer and the euphotic zone (**Figs. 5c, 5d, and 5f**). This signal was also present in the  
354 backscatter at 650 nm (Fig. 5h). While the higher concentration on the backscatter is evident offshore at  
355 the surface ( $\sim 4.5 \times 10^{-4} \text{ m}^{-1}\text{sr}^{-1}$ ) and decreases with depth and proximity to the shore, in the same area  
356 as the elevated CHL and DO, the backscatter reaches values  $\sim 3 \times 10^{-4} \text{ m}^{-1}\text{sr}^{-1}$ , whereas in the  
357 surrounding waters it is less than  $2 \times 10^{-4} \text{ m}^{-1}\text{sr}^{-1}$ . This aligns with subduction of CHL (**Fig. 5g**) and  
358 backscatter at 650 nm (**Fig. 5h**) along the isopycnals between 28.2-28.3  $\text{kg/m}^3$  below the mixed layer and  
359 Zeu (120 m) at depths greater than 200 m, contributing to the export of organic matter as it has been  
360 observed in other regions of the global ocean (Zarokanellos et al., 2022; Zarokanellos and Jones, 2021;  
361 Erickson et al., 2016)

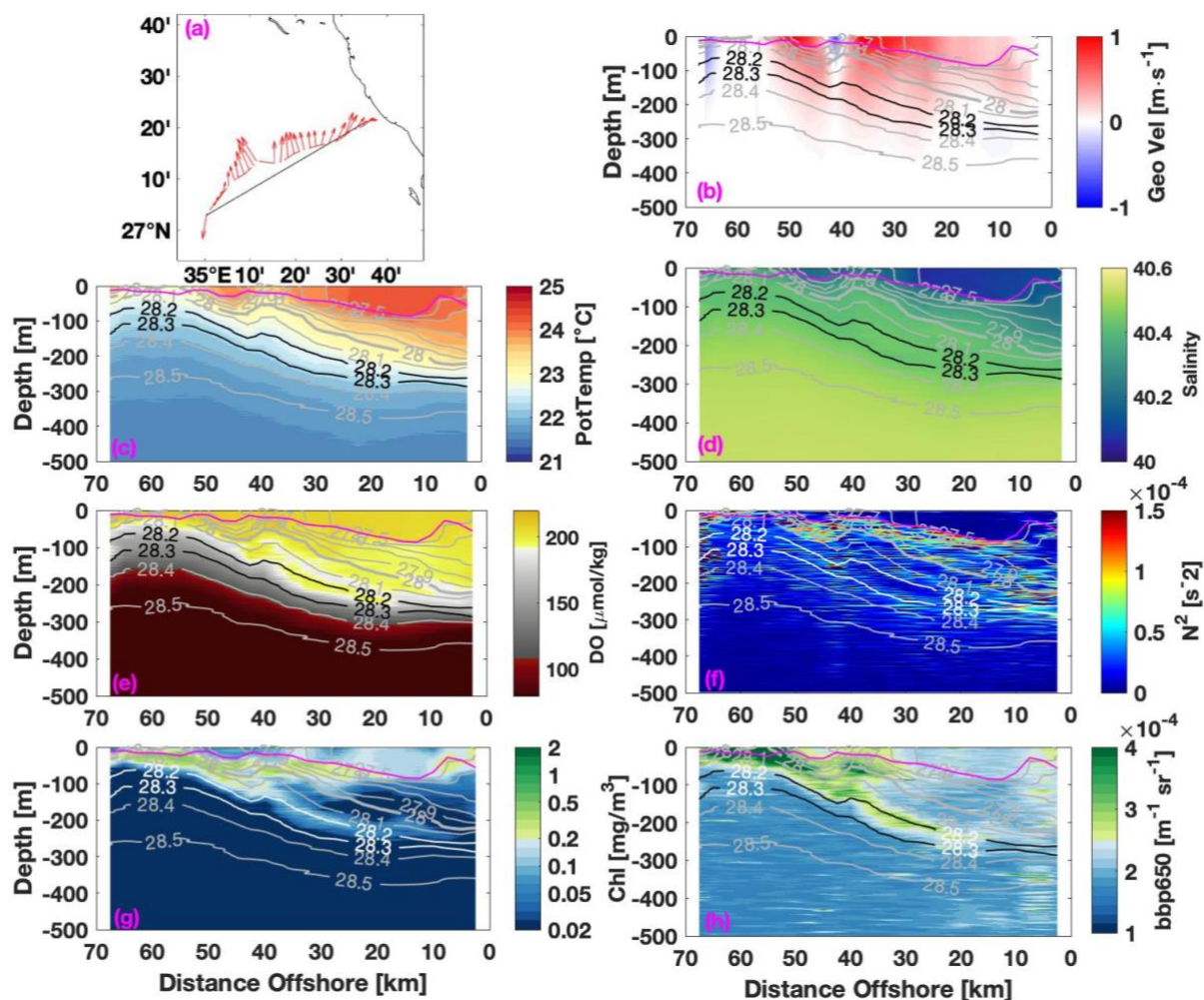


**Fig. 5:** Glider section of a) Depth Averaged Current (DAC), b) Geostrophic velocity, c) Potential temperature, d) Salinity, e) Dissolved Oxygen, f) Brunt-Väisälä frequency, g) Chlorophyll-a, and h) Backscattering coefficient at 650 nm, for February 5–9, 2019. Density isopycnals are shown in subfigures b, c, d, e, f, g, and h with solid grey lines, while the isopycnals of 28.2 and 28.3 are distinguished with black lines (or white for f, g, h). The solid magenta line represents the MLD. Geostrophic velocity, calculated relative to 500 m, is positive to the north-northwest and negative to the south-southeast parallel with the coastline.



371 The glider observations of CHL, backscatter at 650, and DO allow us to independently trace the  
372 subduction with three different bio-optical tracers. Indeed, the observed elevated CHL—commonly  
373 associated with phytoplankton growth in the literature—primarily occurs only offshore, within the Ze,  
374 where dense water ( $\geq 28.1$  kg/m<sup>3</sup>) rose to a depth shallower than 50 m, bringing up nutrients from deeper  
375 layers. Also, the Zeu is located around 120 m in the RS, and light at greater depths is too low to sustain  
376 photosynthesis (Zarokanellos and Jones, 2021). Furthermore, this transient eddy about 43 km offshore  
377 was not observed in either the previous or the following section, and it was embedded within the larger-  
378 scale flow (**Figs. 5a, 5b, and 5e**). The observed high DO concentration on the surface can be a result of  
379 photosynthesis. The co-occurrence of high CHL and DO at depths below the Zeu suggests that this water  
380 was originally at the surface before it transferred and subducted deeper. The fact that the high CHL and  
381 DO waters align along the 28.2 isopycnal (**Figs. 5, 11a, and 11b**) indicates that their subduction is  
382 associated with an eddy wherein the denser surface water is forced below, with the lighter water following  
383 the 28.2 isopycnal rather than being vertically mixed

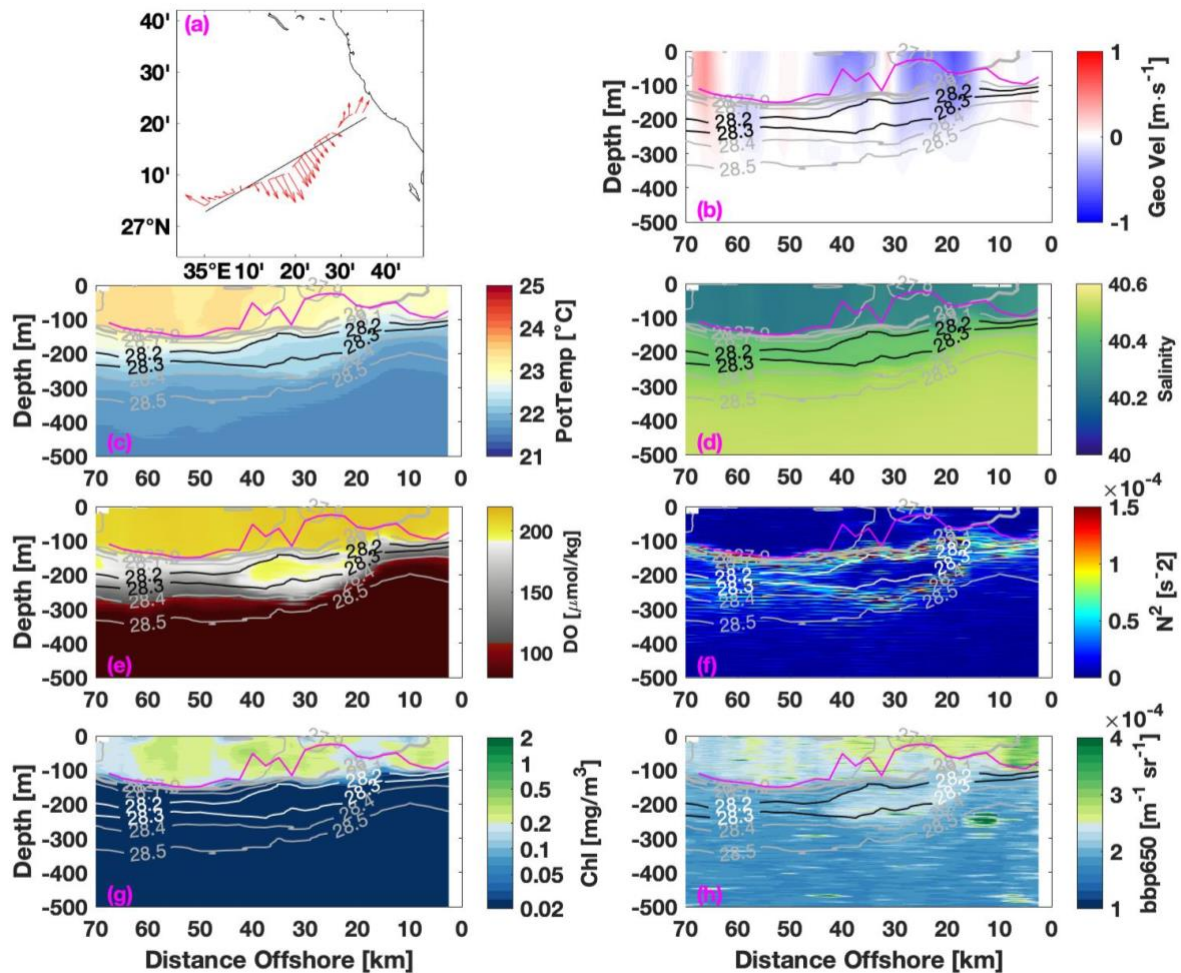
384 Following the initial period of northward transport, the circulation changed significantly in late  
385 February, reversing the direction of flow across the glider line due to the presence of an AE in the north-  
386 eastern RS (**Figs. 3d-f and 6**). Based on glider sections, the southward coastal flow began in mid-February  
387 and persisted for approximately 3 weeks. The isopycnal structure associated with the anticyclonic  
388 geostrophic flow is evident below the mixed layer. In the glider section from March 1–5 the geostrophic  
389 velocity varied between weakly northward at the offshore and inshore ends of the line to a maximum  
390 southward velocity of 0.67 m/s southward, and an average southward velocity of 0.14 m/s in the upper  
391 100m, weaker in magnitude than the northward flow during the preceding cyclonic period (**Fig. 6b**).  
392 During this period, the upper boundary of the pycnocline, 28 kg/m<sup>3</sup>, which had been near the surface  
393 offshore during early February, was now at nearly 150 meters depth in the offshore portion of the transect  
394 but rose to the surface near the coast (**Fig. 6**). The MLD was consistently deeper than 100 meters in the  
395 offshore 30 km of the transect, and in the near-shore 40 km, it varied between ~25 and 120 m. CHL was  
396 uniformly distributed within the mixed layer with diel patterns in concentration, which appear as spatial  
397 patterns in the 3.5-day transit of the line (**Fig. 6g**).

398 Typically, the oxygenated waters are located in the surface layers within the MLD. However, the  
399 observed bolus indicated that high oxygenated waters had trapped below the MLD, between the 28.2 and  
400 28.3 kg/m<sup>3</sup> isopycnals at 150 to 250 m depths and between 20 and 50 km offshore. The average DO  
401 concentration within the bolus is ~177 µmol/kg, while CHL is around  $4.6 \times 10^{-3}$  mg/m<sup>3</sup>. The surrounding  
402 waters below the 28.3 isopycnal indicate that the DO and CHL values reach 62 µmol/kg and  $2.9 \times 10^{-3}$   
403 mg/m<sup>3</sup>, respectively. Above the 28.2 isopycnals, the DO and CHL have values of 203 µmol/kg and  $79 \times$   
404  $10^{-3}$  mg/m<sup>3</sup>, correspondingly. Compared to the underlying layers, CHL within the bolus is slightly  
405 elevated (~3.6%), while DO is significantly higher by approximately 285%. The thickness of the layer  
406 between these two isopycnals varies, ranging from less than 40 m, and the thickness of the trapped bolus  
407 is approximately 100 m, indicating a distinct water mass that is also associated with low BVF. The  
408 observed elevated BVF around the bolus suggests that this is a stable water mass isolated from the  
409 surrounding water column rather than a result of vertical mixing. This lens is slightly warmer (~22.3°C)  
410 and more saline (~40.43) than other waters within the same isopycnal range along the transect (**Fig. 6c,**  
411 **6d, 6f**). While its signature was not reflected in CHL (**Fig. 6g**), the bolus is also detectable in backscatter  
412 (**Fig. 6h**), with a concentration nearly 11% higher than the surrounding waters (**Fig. 6h**). This bolus is  
413 likely outflow water from the Gulf of Aqaba, which might be advected into the region by the southward  
414 flow and subsequently captured and recirculated by the observed AE (**Fig. 6a**). Only a few studies are  
415 available regarding the water mass characteristics of the Gulf of Aqaba (Manasrah, 2002; Manasrah et  
416 al., 2004), suggesting that the upper 300 m of the Gulf exhibit conditions similar to those found in the  
417 upper 100 m of the NRS during winter, with temperatures ranging from 20.4°C to 22.4°C and for the  
418 salinity between 40.3 and 40.7.

419 The near-surface temperature continued to decrease through March, while salinity increased within  
420 the surface layer, reaching a maximum salinity of 40.4 and a density anomaly of about 28.4 kg/m<sup>3</sup> in late  
421 March (**Fig. 4**). The corresponding glider section of temperature and salinity for this period (**Figs. 7c-d**),  
422 March 26–29, shows that the coolest, saltiest, and densest water occurred in the center of a cyclonic eddy  
423 about 40–45 km offshore, where the dense isopycnals (>28.2 kg/m<sup>3</sup>) outcrop at the surface. Across this  
424 transect, the near-surface temperature was less than 22.8 °C, the minimum salinity was more than 40.3,  
425 the minimum near-surface density was >28 kg/m<sup>3</sup>, and the minimum stratification was  $<1 \times 10^{-4}$  (**Fig. 7f**).



426 Prior to this, the shallowest that the  $28.2 \text{ kg/m}^3$  isopycnal was observed was in the early section between  
 427 February 5 and 9, at a depth of about 90 m at the offshore end of the transect. In the same transect, the  
 428 isopycnal descended below 250 m nearshore. Mixed layer depth along this transect ranged from as  
 429 shallow as 12 m to as deep as 148 m on the inshore end of the transect, on the periphery of the eddy  
 430 circulation. In the eddy center, the mixed layer extended to the depth of the  $28.3 \text{ kg/m}^3$  isopycnal where  
 431 stratification due to the uplifted pycnocline impeded deeper mixing. The isopycnal uplifting appears to  
 432 be in the center of a cyclonic feature where the geostrophic velocity (**Fig. 7a, 7b**) is northward nearshore  
 433 (0.5 m/s) and southward offshore (0.2 m/s)



434  
 435 **Fig. 6:** Same as for **Fig. 5**, but for the period of March 1–5, 2019

436 As in earlier sections, small-scale structures are apparent and potentially important to biogeochemical  
437 processes. At about 20 km offshore, a low DO and low CHL feature extends upward from about 200 m  
438 to at least 100 m depth (**Figs. 7e-g**). The low DO concentration extends to shallower depths. The uplift of  
439 isopycnals affects the biogeochemical processes by bringing low DO and CHL waters into the Zeu. This  
440 process modulates nutrient, carbon, and DO availability and ultimately affects primary production.  
441 Phytoplankton growth depends on the nutrients and light availability. The low-CHL waters typically  
442 indicate nutrient-depleted conditions at the surface, while the low-DO waters in deeper layers are  
443 generally enriched with remineralized nutrients such as nitrate, phosphate, and silicate (Garcia H.E. et al.,  
444 2018). In this case, the low-CHL and DO waters have reached  $\sim 60$  m, penetrating the Zeu, which extends  
445 to  $\sim 120$  m, as reported by Zarokanellos and Jones (2021). When these nutrient-available waters reach  
446 the Zeu, they can stimulate phytoplankton blooms, enhancing primary production (Falkowski et al.,  
447 1998). The uplift of the 28.3 isopycnal ( $\sim 60$  m) due to the presence of the cyclonic eddy (**Fig. 7**), also  
448 influences nutrient availability (Zarokanellos & Jones, 2021; Kurten et al., 2019). This mesoscale eddy  
449 activity in the region often drives the shift in the phytoplankton community (Kurten et al., 2019).

450 The presence of the CE leads to an uplift of the isopycnals about 50 km offshore (**Fig. 7**). In the  
451 shoreward periphery of this eddy ( $\sim 20$  km offshore), both CHL and DO penetrate to a depth of up to 250  
452 m, well below the mixed layer and the Zeu depth (**Figs. 7g and 7e**). This subduction occurs near the  
453 nearshore reversal of flow. Unfortunately, no backscatter data were acquired during this period (**Fig. 7h**).

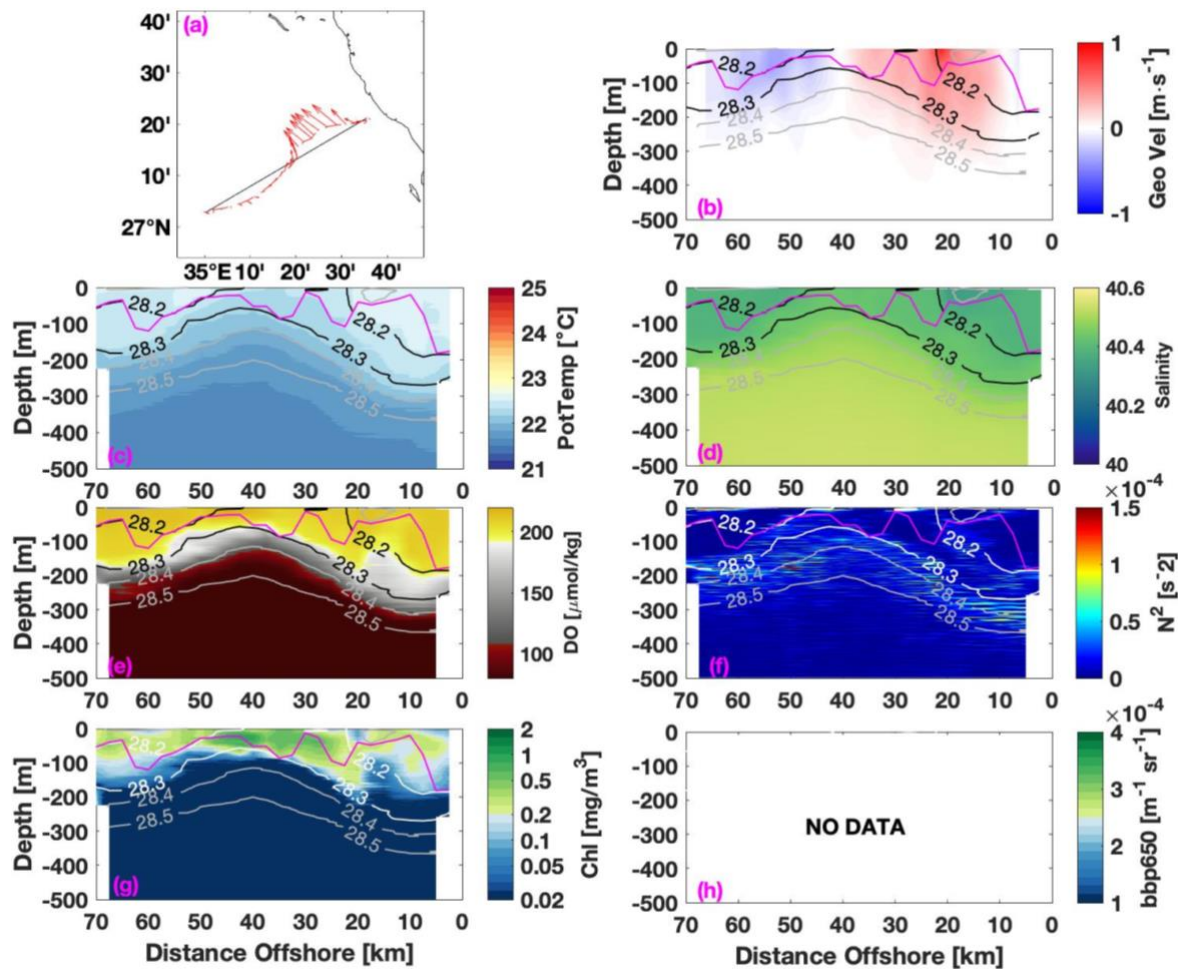
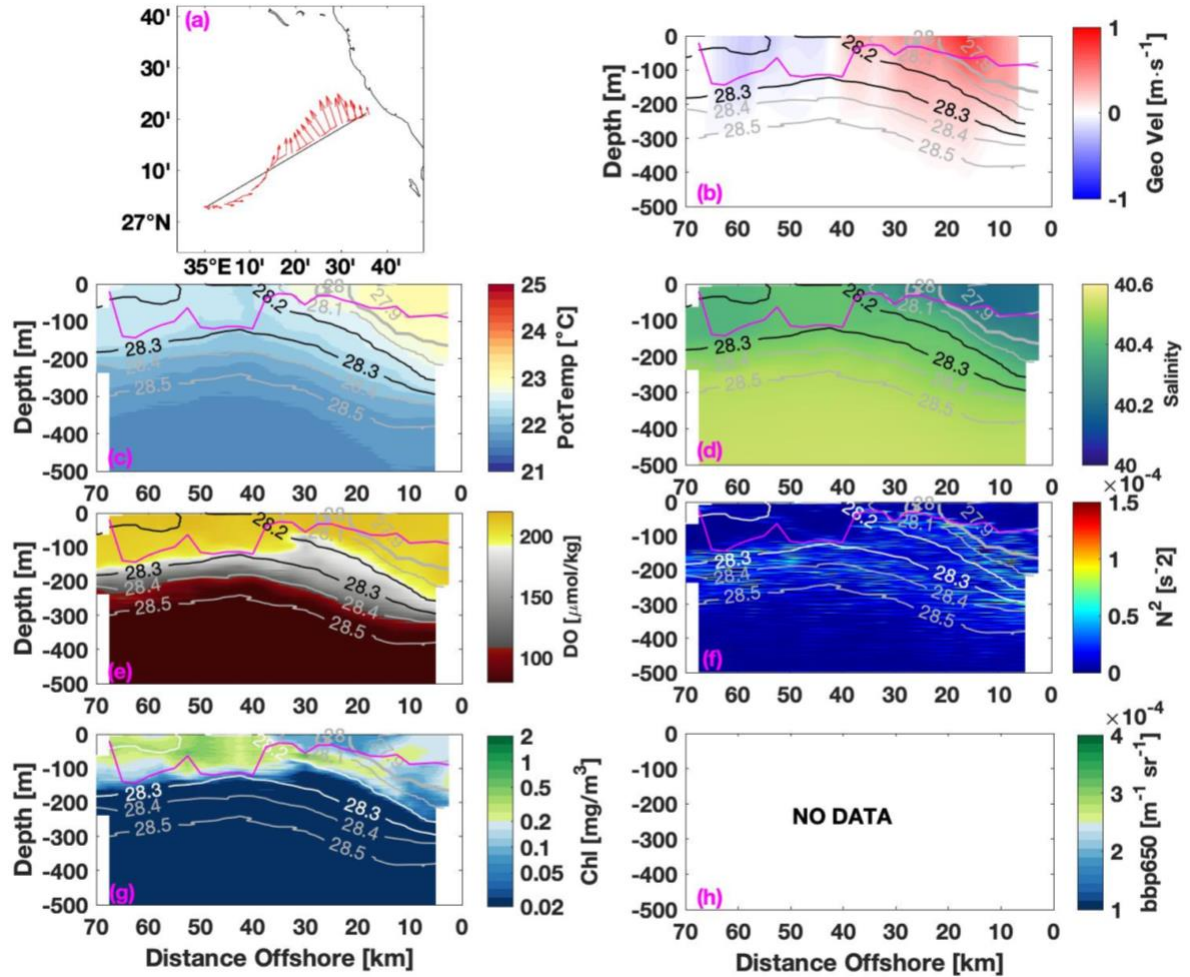


**Fig. 7:** Same as for **Fig. 5**, but for the period of March 26–29, 2019.

Immediately following this cool period, warmer, fresher water began to appear in the nearshore region of the glider line (**Figs. 8c-d**). The shallowing of lower-oxygen water, hence nutrient-rich, offshore between 35 and 50 km was observed in late March and subsided with the weakening of the cyclonic circulation (**Fig. 8e**). The cyclonic circulation remained (**Fig. 8a**), but it was entraining the warmer, fresher water from the south, as is evident in the composite SST image from March 30–April 6 (**Fig. 3k**). This warming and freshening continued through the remainder of the glider deployment (**Fig. 4a**). Freshening was evident on the nearshore half of the glider line, where salinities fell below 40.3, while

465 remaining higher along the offshore half of the line. Denser water subsided except at the outer half of the  
 466 transect. Although the direction of the geostrophic velocity was similar in pattern to the previous period  
 467 (**Fig. 7e**), the magnitude of the nearshore flow intensified by 0.2 m/s, while the offshore flow was similar  
 468 to the previous transect (**Fig. 8b**). **Fig. 8g** shows that the CHL concentration between 35 and 50 km  
 469 offshore decreased as warmer water was entrained near the coast.

470 Subduction is also present between 30 and 10 km onshore and is clearly observed in the BVF panel  
 471 and in CHL and DO (**Figs. 8b, 8e, and 8g**). The subduction displaces the pigments of CHL and DO deeper  
 472 than 200 m nearshore; in the offshore area, these two parameters are well distributed in the first 100 m.  
 473



474  
 475 **Fig. 8:** Same as for **Fig. 5**, but for the period of March 29-April 2, 2019.

#### 4. Discussion

The NRS is a dynamic and complex three-dimensional circulation with significant seasonal variability influenced by strong atmospheric forcing through wind stress and air-sea buoyancy fluxes. Direct observations and modeling experiments have both captured the formation of locally produced intermediate (RSOW) and deep water (RSDW) masses and their interactions with adjacent gulfs of Suez and Aqaba (Table 2; Asfahani et al., 2020; Sofianos and Johns, 2003; Papadopoulos et al., 2015). Two main thermohaline cells are associated with water mass formation and influenced by mesoscale dynamics, wintertime cooling, and deep convection. Numerical simulation studies suggest that the cyclonic gyre is the most probable site for RSOW formation (Yao et al., 2014a; Sofianos and Johns, 2003).

Unlike previous observations and interpretations of the NRS (e.g., Asfahani et al., 2020; Papadopoulos et al., 2015; Yao and Hoteit, 2018), this study observed a reversal of the currents in the eastern half of the basin prevented the inflow of warmer, fresher water from the south. During this phase, the upper layer of the NRS became relatively homogeneous, and near-surface water along the glider line reached its maximum salinities and densities (**Figs. 5d** and **7d**).

To evaluate the similarities and differences with previous years, an EOF analysis was performed on the SLA data between 26 °N and 28 °N over a period of 4 years that has been considered efficient (from 2016 to 2019; **Fig. 9**). The first mode of the EOF describes 86.6 % of the SLA variation (**Fig. 9a**). In the years 2016–2018, the EOF of the SLA showed a relatively positive or neutral pattern during the winter-spring transition period, which continued until May, when the EOFs typically decreased (**Fig. 9b**). This late spring decrease generally coincides with the transition from a net negative air-sea heat flux to a net positive flux (see **Fig. 2b**). For 2019, the first mode of the EOF showed a distinct increase in late January through mid-February, then became negative through mid-March, in contrast to the pattern in previous years. This negative phase is consistent with the period when the circulation was anticyclonic (**Fig. 9b**). The flow of warmer, fresher water from the south was apparently blocked during this period, and the temperature became relatively homogeneous in the NRS, as have been previously observed in the CRS (Zarokanellos et. al., 2017). Recently, a study by Mohamed and Skliris (2025) showed that the annual climatology of the sea level is generally higher on the eastern boundary of the RS compared with the western boundary, where many areas are isolated patches of higher or lower values of SLA indicate



mesoscale activity. The maximum values correspond with regions where AEs are present. In our study, the negative phase of the EOF analysis (**Fig. 9b**) aligns with the presence of AE in the NRS.

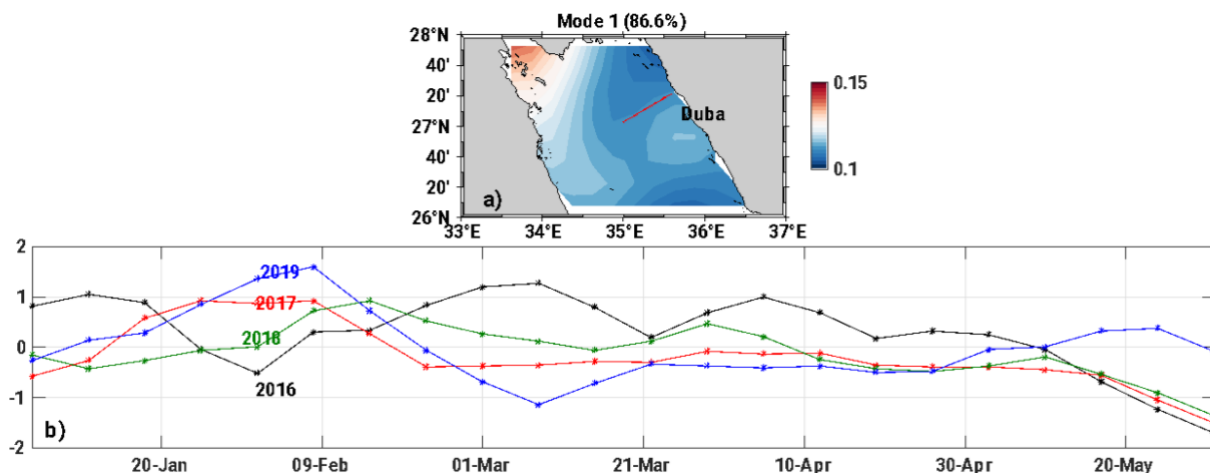


**Fig. 9:** The first mode of the EOF based on the SLA weekly mean in 2019. (a) the spatial pattern of the first mode. (b) time series graph of the first mode for four (4) subsequent years: 2016 (black), 2017 (red), 2018 (green), and 2019 (blue) from January to May.

We examined the relationship between the first mode of the EOF and atmospheric forcing using a time-lagged correlation. No clear correlation was discernible from this analysis (not shown). But in comparison with the previously published observations from 2016 (Asfahani et al., 2020), the period of negative average heat flux lasted longer into the spring. Thus, there is an overall difference in the duration of the negative heat flux between the 2016 observations and the observations in 2019.

The surface layers responded to the heat loss with decreased temperatures and increased salinity and density. The cumulative effect of the cooling through the entire winter period resulted in the formation of the densest surface waters in late March, when the difference in temperature and salinity between the surface and the deep layers was at a minimum. Following this cooling phase, the net heat flux fluctuated around zero. Then in early April, the weakening of the atmospheric forcing, the transition to positive heat fluxes, and restratification due to advection from the south resulted in a near-surface temperature increase of 1°C and a salinity decrease of 0.2, both of which contributed to the near-surface density decrease in April (**Fig. 4**). The warmer, less saline, and thus lighter water from the south spread into the area, and

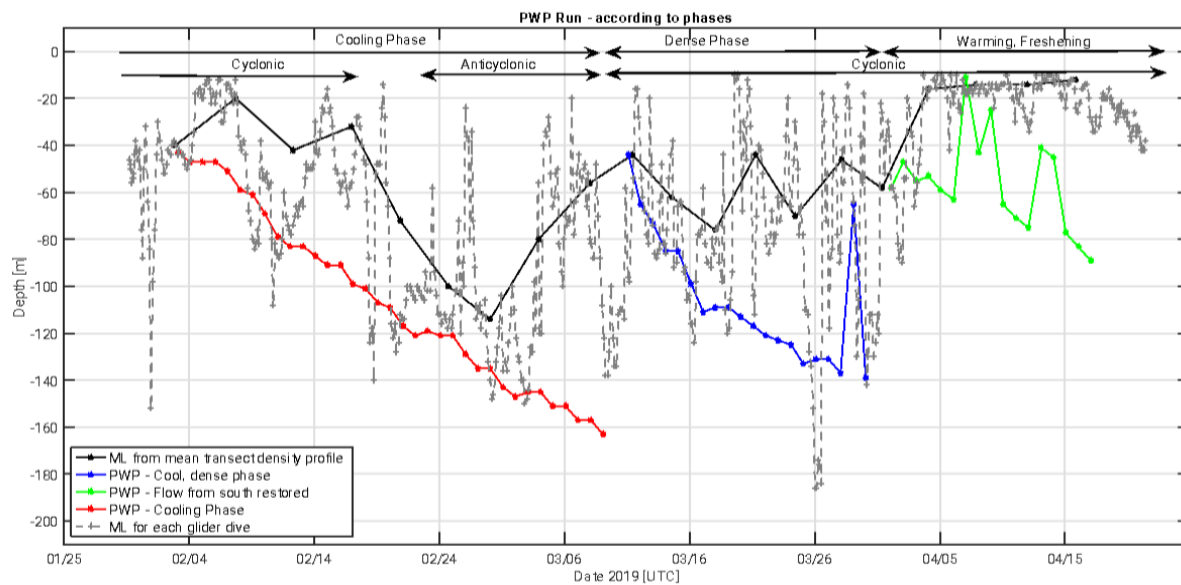
during the restratification, it overrode the denser waters, isolating them from additional direct ocean-atmospheric interaction.

The water underlying the more buoyant surface water, which lies along the 28.2 kg/m<sup>3</sup> isopycnal, extended from the surface in mid-transect to approximately 200m nearest the coast (**Fig. 8**). This recently exposed subsurface water spreads in the basin, and its signal can be detected in the CRS, as mentioned by Zarokanellos and Jones (2021). This water results from the northward advection of GASW, which is subjected to evaporation along its entire transit of the RS. Winter cooling throughout the entire period further modifies the transported surface water in the NRS. During this particular year, the presence of the AE in the NRS temporarily blocked advection from the south, contributing to the surface waters' extended exposure to the atmosphere. Near the end of the cooling period, when the surface water reached its maximum density, the cyclonic circulation was reestablished, contributing to the inflow of buoyant GASW which overlaid the denser water.

In this study, the PWP model was applied to subsets of the observational period to further understand the relationship between the local heat flux and the advection of water from the south. The PWP model used daily surface heat flux and wind stress, as a pronounced diurnal cycle was not evident in the observed salinity and temperature data. While this simple 1-dimensional model cannot capture the spatial variability of the water column structure or the atmospheric forcing field, it effectively illustrates the role of atmospheric forcing in driving the seasonal evolution of the mixed layer in the absence of these complexities. In contrast, Krokos et al. (2022) used a 4-dimensional MIT-GCM model to investigate the spatial and seasonal evolution of mixed layer variability across the entire RS, highlighting the critical role of atmospheric forcing, particularly through its influence on mixed layer temperature. This broader modeling approach supports the atmospheric-driven dynamics demonstrated by our PWP findings.

**Fig. 10** shows the evolution of the MLD in the upper 200 m based on the PWP simulation. Three separate PWP simulations were performed, initiating each simulation at the onset of one of the three phases determined from the in-situ observations. The initial temperature and salinity profiles for the model run were taken from the glider section nearest the initiation point of the run. The cooling phase extended from February 1st until March 8th (35 days). During this period, first presence of a mesoscale cyclonic

550 eddy and later an anticyclonic eddy in the study area were observed. In the same period, the simulated  
551 MLD is constantly deepening, reaching a maximum depth of 162m at the end of the cooling phase.  
552 During the dense phase, the observed MLD shows large fluctuations and mismatches with the  
553 simulated MLD. The 1-D model failed to capture the shallowing of MLD during the dense phase. The  
554 observed discrepancy is based on the pycnocline depth that shallowed substantially, such that the dense  
555 pycnocline intersected with the surface. Lastly, the PWP-simulated MLD during the warming phase also  
556 shows a discrepancy with the observed MLD. During this phase, the observed MLD rapidly shallowed to  
557 less than 45 m, and the mean MLD was about 20 m. The shallowing of the MLD during the warming and  
558 freshening phases was attributed, in part, to the northward flux of the buoyant Gulf of Aden Water. But  
559 the shallowing of the pycnocline due to the cyclonic eddy also contributed to the shallowing of the MLD,  
560 as seen clearly in **Fig. 8**. In addition, the shallowing of the MLD due to the presence of the CE facilitates  
561 exporting the surface water masses to the deeper layers below the euphotic zone, as indicated from the  
562 backscatter (**Fig. 5 h**).



563  
564 **Fig. 10:** Comparison between the observed transect-averaged MLD from the glider (black) and PWP-  
565 simulated MLD during the 1) cooling phase (red), 2) cool-salty and dense phase (blue), and 3) warming-  
566 freshening phase (green). The black + symbol shows the MLD for each dive, interconnected by the black  
567 dashed line.



568

569 Water mass subduction along isopycnals is a component of the formation of RSOW during winter  
570 and a contributor to the carbon flux from the Zeu to the interior of the RS. As shown in **Fig. 5**, a water  
571 mass containing elevated CHL and DO can extend well below the mixed layer and Zeu. Although only  
572 one example with this feature (February 5-9, **Fig. 5**) is shown in this paper. Subducted water was evident  
573 in the glider deployment from its deployment on January 30 through the fourth transect that was  
574 completed on February 18. Key characteristics of this feature were elevated CHL and DO on the 28.2  
575 kg/m<sup>3</sup> isopycnal that extended to as deep as 250 meters. In **Fig. 5**, this feature was evident from about 45  
576 km offshore and shoreward. **Fig. 11** shows the relationship between these variables and density between  
577 20 and 40 km offshore. A clear peak in both variables aligns with the 28.2 kg/m<sup>3</sup> isopycnal. Inshore, at  
578 45 km, the region between 150 and 500 m contains a measurable fraction of the total CHL. In addition,  
579 **Fig. 11d** shows that the subduction event contributes 20% to the integrated CHL between 150 and 500m.

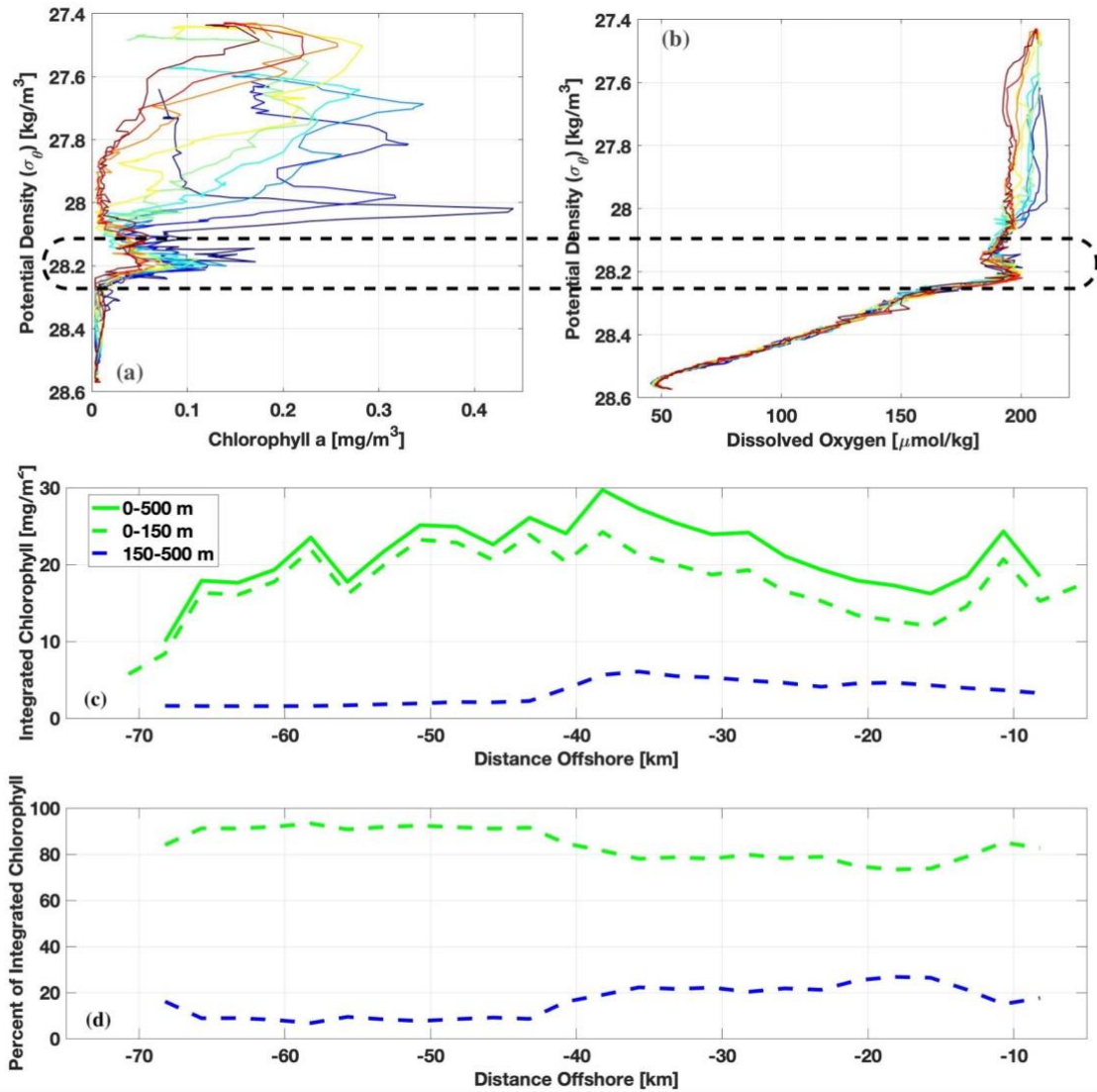
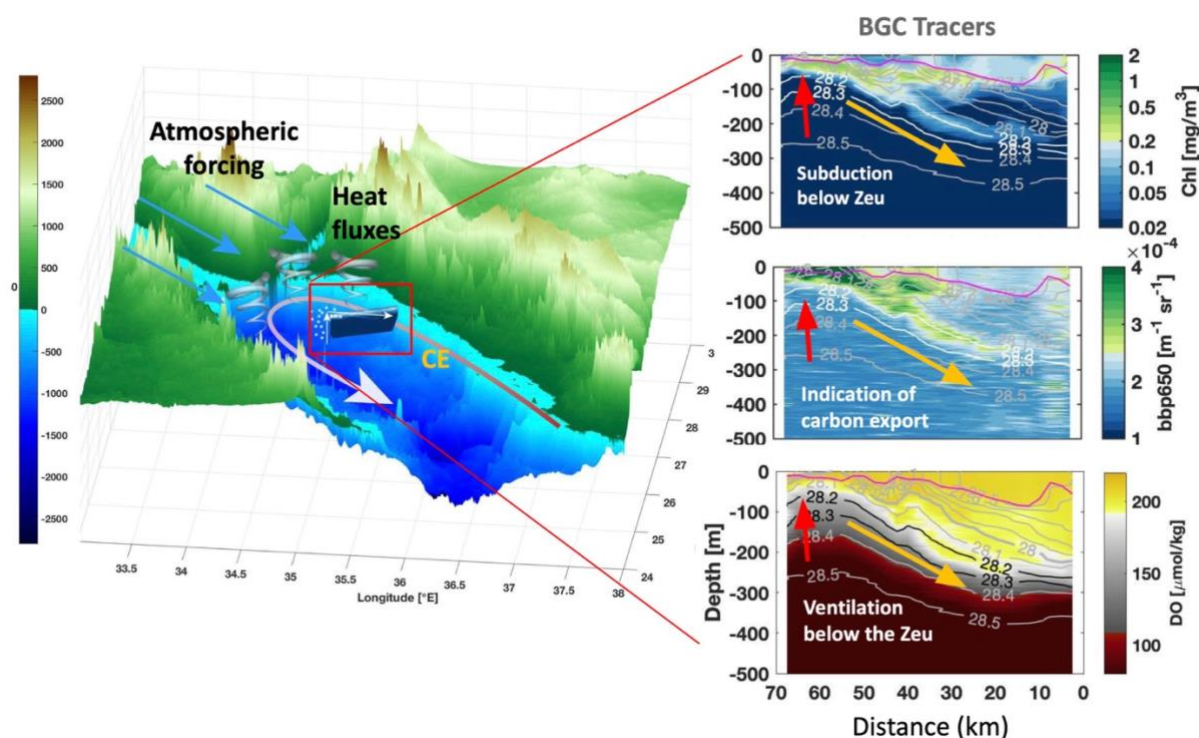


**Fig. 11:** Characteristics of the subducted feature in transect 2, February 4–9 (**Fig. 5**). Panels a and b show the concentrations of chlorophyll and dissolved oxygen as a function of density for profiles between 20 and 40 km offshore. Panel c shows the integrated chlorophyll as a function of distance offshore. The solid green line is the total integrated chlorophyll between the surface and 500 meters. The dashed green line is the integrated chlorophyll between the surface and 150 m, and the blue line is the integrated chlorophyll between 150 and 500 m. Panel d shows the percentage of the integrated chlorophyll from 0 to 150m (dashed green line) and from 150 to 500m (dashed blue line).

589 Given the limitations of our observations, constrained by the Exclusive Economic Zone (EEZ)  
 590 boundary, the full mechanism of the formation of this subducted layer is unclear. One possible mechanism  
 591 is that either vertical mixing or sinking of particles on the western half of the NRS (Kheireddine et al.,  
 592 2020) could create this feature, which is then entrained into the cyclonic circulation in this region and  
 593 transported from the western side of the basin to the eastern side. **Fig. 12** shows a conceptual diagram of  
 594 RSOW subduction and its biogeochemical impact on the NRS based on the existing observations.  
 595 Regardless of the details of the mechanism, subduction is a process that needs to be considered in the  
 596 physical and biogeochemical dynamics of the NRS.



599 **Fig. 12:** Conceptual diagram of RSOW subduction and its biogeochemical impact on the NRS.  
 600 Topographic and bathymetric representation of the study area where physical and atmospheric processes  
 601 superimposed on the map indicate the general cyclonic circulation (grey arrow), the influence of  
 602 atmospheric forcing (blue arrows), and heat fluxes (grey spirals; left panel). Panels on the right display  
 603

604 the glider section of CHL (top), backscatter at 650 nm (middle), and DO (bottom). Red rows correspond  
605 to the uplifting of the isopycnal and yellow arrows to the subduction of the newly formed RSOW.  
606 Subducted CHL, backscatter at 650 nm, and DO are traced below the Zeu (~120 m) associated with carbon  
607 export and ventilation of the deeper layers. The green isopleth of 180  $\mu\text{mol/kg}$  presents the nitracline  
608 (bottom-right panel).

## 5. Conclusion

The primary objective of this study was to understand the mechanisms contributing to the water mass formation of RSOW in the NRS and the associated biogeochemical responses. Our findings demonstrate that the RSOW formation is closely linked to the presence of a cyclonic eddy and intense winter cooling, consistent with previous studies (Asfahani et al., 2020; Sofianos and Johns, 2003; Papadopoulos et al., 2015; Yao et al., 2014b). A novel finding of this study is the role of water mass subduction, which, although not previously discussed, contributes not only to the RSOW formation but also to the carbon export as CHL and backscatter indicated that water has been subducted below the Zeu (**Fig. 12**). The observations also indicate that subduction events can significantly contribute to the ventilation of intermediate and deeper waters, thereby affecting the overall oxygen budget of the RS. During these events, oxygen-rich surface waters are transported into subsurface layers along the 28.2 kg/m<sup>3</sup> isopycnal, facilitating oxygen redistribution at depth. The study also identified a transition from negative to positive heat flux and the re-establishment of northward flow along the eastern RS coast, signalling the cessation of the RSOW formation as less dense water from the south caps the denser northern waters. The presence of the AE south of the study area prevented the advection of more buoyant surface water. Although we could not determine the mechanism for this reversal of CE to AE from our observations and 1D model simulations. This likely influenced the observed water mass originating from the northern gulfs within the RSOW density range, consistent with Papadopoulos et al. (2015). This study highlights that multiple factors can contribute to RSOW formation (**Table 2**), including dense isopycnal surfacing from cyclonic circulation, vertical mixing, dense outflow from the northern gulfs, water mass subduction, the extension of dense isopycnal exposure due to blockage of buoyant flux from the south, and the eventual termination of these processes as the buoyancy flux is restored. In addition, it is clear that the submesoscale features are present in the region and contribute to the overall physical and biogeochemical dynamics of the region. To comprehensively capture the spatial and temporal dynamics of RSOW formation, future research should prioritize detailed observational and modeling studies, integrating autonomous platforms and ship-based sampling across the entire NRS basin. Such an approach would resolve the three-dimensional variability and provide valuable insights into the sources and sinks involved in RSOW formation and its biogeochemical impacts.

Contributing Mechanisms	Yao et al 2014 (a & b)	Papadopoulos et al 2015	Asfahani et al 2021	Krokos et al 2022	This Study
Cyclonic Circulation leading to exposure of dense isopycnals	√	√	√		√
Convective mixing	√	√	√	√	√
Upwelling/Downwelling along boundaries	√				
Outflow from Gulfs		√			√
Along basin pressure gradients	√				
Submesoscale processes					√
Subduction of dense water from surface water into pycnocline					√
Anticyclonic blockage of northward flow of buoyant water into NRS					√
<b>Biogeochemical effects</b>					
Eddy driven upwelling nutrient flux		√	√		√
Convective mixing nutrient flux into euphotic zone			√		√
Subduction results in the downward transport of dissolved oxygen and					√

particulate carbon below the euphotic zone					
--	--	--	--	--	--

**Table 2:** Summary of the major conclusions from the related studies relative to the formation of the RSOW in NRS.

## **Data availability**

The data sets that are presented in this paper (glider time series and gridded sections, 8-day remotely sensed SST, chlorophyll, and sea level anomaly/geostrophic velocity, and the NASA MERRA-2 reanalysis data) are available through the Zenodo repository (<https://doi.org/10.5281/zenodo.11046900>) <https://zenodo.org/records/11046900?preview=1&token=eyJhbGciOiJIUzUxMiJ9.eyJpZCI6IjA4ZDdkMzY0LTQyMGUtNGRiYS1iYTVmLWRkYjhlM2M2M2I2YyIsImRhdGEiOnt9LCJyYW5kb20iOiI2MWM1YjUyOGQxZDBkYmRkOTc5MjI4MDYxZWVhZGkzDwCZ1576vzMKco mKl4Zax-uy9lbG XHE1zfT ag31O5DHNh0VHlJWQnxfn0S3HBbOXS 2QhoPTbDQ.>

## **Author contribution:**

All authors have contributed to Conceptualization, Data Curation, Formal Analysis, Investigation, Writing – original draft preparation and Writing – review & editing. Visualization is done by L.E., Z.K. and B.H.J.. Software is done by L.E. and B.H.J.. while supervision is done by Z.K. and B.H.J.

## **Competing interests**

The authors declare that they have no conflict of interest.

## **Acknowledgements**

The authors gratefully acknowledge the NASA Goddard Space Flight Center, Ocean Ecology Laboratory, Ocean Biology Processing Group for remote sensing data and the Copernicus website for the SLA data used in this study. The authors are grateful to the KAUST Coastal Marine Resources Core Lab (CMRCL) for their engineering and field support during the glider operations. Particular thanks go to Thomas Hoover, Samer Mahmoud, Mohammed A. Aljahdli and Lloyd Smith for their help with the glider deployments. The authors are also grateful to Dr. Luc Rainville for his suggestions and discussions regarding the PWP implementation. This research was supported by King Abdullah University of Science and Technology (KAUST) University. The ocean color products were obtained from NASA Ocean Color Group. The data are freely available online through the official website <https://oceandata.sci.gsfc.nasa.gov/directdataaccess/Level-3%20Mapped/Aqua-MODIS/2019/>.



The altimeter products were produced by Ssalto/Duacs and distributed by Aviso+, with support from Cnes (<https://www.aviso.altimetry.fr>). Dataset accessed [2022-01-27] at 10.5067/MODAM-8D4N9. The SST data source is NASA OBPB. 2020. MODIS Aqua Global Level 3 Mapped SST. Ver. 2019.0. PO.DAAC, CA, USA. MODIS CHL level 3 data was obtained via <https://oceancolor.gsfc.nasa.gov/cgi/l3>. We would like to acknowledge that the author Z.K. was partially part of the ITINERIS project.

### Financial support

We thank the EU—Next Generation EU Mission 4 “Education and Research”—Component 2: “From research to business”—Investment 3.1: “Fund for the realisation of an integrated system of research and innovation infrastructures”—Project IR0000032—ITINERIS—Italian Integrated Environmental Research Infrastructures System—CUP B53C22002150006 for partially funding the author Z.K.

### References

Abualnaja, Y., V. P. Papadopoulos, S. a. Josey, I. Hoteit, H. Kontoyiannis, and D. E.: Raitsos Impacts of Climate Modes on Air-Sea Heat Exchange in the Red Sea, *Journal of Climate*, 28(7), 2665–2681, doi: 10.1175/JCLI-D-14-00379.1, 2015.

Asfahani, K., G. Krokos, V. P. Papadopoulos, B. H. Jones, S. Sofianos, M. Kheireddine, and I. Hoteit: Capturing a Mode of Intermediate Water Formation in the Red Sea, *Journal of Geophysical Research: Oceans*, 125(4), e2019JC015803, <https://doi.org/10.1029/2019jc015803>, 2020.

Al Senafi, F.; Anis, A.; Menezes, V. Surface Heat Fluxes over the Northern Arabian Gulf and the Northern Red Sea: Evaluation of ECMWF-ERA5 and NASA-MERRA2 Reanalyses. *Atmosphere*, 10, 504. <https://doi.org/10.3390/atmos10090504>, 2019.

Beal, L. M., A. Ffield, and A. L. Gordon: Spreading of Red Sea overflow waters in the Indian Ocean, *Journal of Geophysical Research*, 105(C4), 8549–8564, doi:10.1029/1999JC900306, 2000.

Biton, H. Gildor, and W. R. Peltier: Red Sea during the Last Glacial Maximum: Implications for sea level reconstruction, *Paleoceanography*, 23, PA1214.doi:10.1029/2007PA001431, 2008.

695 Biton, Gildor, Trommer, Siccha, Kucera, van der Meer, and Schouten: Sensitivity of Red Sea  
696 circulation to monsoonal variability during the Holocene: An integrated data and modelling study,  
697 *Paleoceanography*, 25(PA4209), 1-16, doi:10.1029/2009PA001876, 2010.

698 Bower, A. S., and J. T. Farrar: Air-Sea Interaction and Horizontal Circulation in the Red Sea, in *The*  
699 *Red Sea*, edited by N. M. A. Rasul and I. C. F. Stewart, pp. 329-342, doi:10.1007/978-3-662-45201-1\_19,  
700 2015.

701 Bower, A. S., and H. H. Furey: Mesoscale eddies in the Gulf of Aden and their impact on the spreading  
702 of Red Sea Outflow Water, *Progress in Oceanography*, 96(1), 14-39, doi:10.1016/j.pocean.2011.09.003,  
703 2010.

704 Cember, R. P.: On the sources, formation, and circulation of Red Sea deep water, *Journal of*  
705 *Geophysical Research: Oceans*, 93(C7), 8175-8191, doi:10.1029/JC093iC07p08175, 1988.

706 Chen, C., Li, R., Pratt, L., Limeburner, R., Beardsley, R. C., Bower, A., Jiang, H., Abualnaja, Y., Xu,  
707 Q., Lin, H., Liu, X., Lan, J., & Kim, T.: Process modeling studies of physical mechanisms of the formation  
708 of an anticyclonic eddy in the central Red Sea, *Journal of Geophysical Research: Oceans*, 119, 1445–  
709 1464. doi:10.1002/2013JC00935, 2014

710 Churchill, J. H., Lentz, S. J., Farrar, J. T., Abualnaja, Y.: Properties of Red Sea coastal currents,  
711 *Continental Shelf Research*, 78, 51–61. doi:10.1016/j.csr.2014.01.025, 2014.

712 Clifford, M., C. Horton, J. Schmitz, and L. H. Kantha: An oceanographic nowcast/forecast system  
713 for the Red Sea, *Journal of Geophysical Research*, 102(C11), 25,101-125,112. doi: 10.1029/97JC01919,  
714 1997.

715 de Boyer Montegùt, C., G. Madec, A. S. Fischer, A. Lazar, and D. Iudicon: Mixed layer depth over  
716 the global ocean: An examination of profile data and a profile-based climatology, *Journal of Geophysical*  
717 *Research*, 109(C12003), doi:10.1029/2004JC002378, 2004.

718 Edwards, A. J., and S. M. Head: *Red Sea, Key Environments Series*, Pergamon Press, Oxford,  
719 doi:10.1016/B978-0-08-028873-4.50008-6, 1987.

720 Emery, W. J.: Water types and water masses, in *Encyclopedia of ocean sciences*, edited, pp. 3179-  
721 3187, Elsevier, doi: 10.1006/rwos.2001.0108, 2001.

722 Erickson, Z. K., A. F. Thompson, N. Cassar, J. Sprintall, and M. R. Mazloff , An advective mechanism  
 723 for deep chlorophyll maxima formation in southern Drake Passage, *Geophys. Res. Lett.*, 43, 10,846–  
 724 10,855, doi:[10.1002/2016GL070565](https://doi.org/10.1002/2016GL070565), 2016.

725 Eshel, M. A. Cane, and M. B. Blumenthal: Modes of subsurface, intermediate and deep-water renewal  
 726 in the Red-Sea, *Journal of Geophysical Research: Oceans*, 99(C8), 15941-15952. doi:  
 727 10.1029/94JC01131, 1994.

728 Eshel, and N. H. Naik: Climatological Coastal Jet Collision, Intermediate Water Formation, and the  
 729 General Circulation of the Red Sea, *Journal of Physical Oceanography*, 27, 1233-1257. doi:  
 730 10.1175/1520-0485(1997)027<1233:CCJCIW>2.0.CO;2, 1997.

731 Eyouni, L., Kokkini, Z., Zarokanellos, N., & Jones, B.. Mechanisms of the Overturning Circulation  
 732 in the Northern Red Sea [Data set]. Zenodo. <https://doi.org/10.5281/zenodo.11046900>, 2024.

733 Fairall, C.W., E.F. Bradley, D.P. Rogers, J.B. Edson, G.S. Young: Bulk parameterization of air-sea  
 734 fluxes for tropical ocean-global atmosphere coupled-ocean atmosphere response experiment, *J. Geophys.*  
 735 *Res.* 101 (C2) 3747–3764 doi: 10.1029/95JC03205, 1996.

736 Falkowski Paul G. et al.,. Biogeochemical Controls and Feedbacks on Ocean Primary  
 737 Production.*Science*281,200-206. DOI:10.1126/science.281.5374.200, 1998

738 Garcia H. E., K.W. Weathers, C.R. Paver, I. Smolyar, T.P. Boyer, R.A. Locarnini, M.M. Zweng, A.V.  
 739 Mishonov, O.K. Baranova, D. Seidov, and J.R. Reagan: World Ocean Atlas 2018, Volume 3: Dissolved  
 740 Oxygen, Apparent Oxygen Utilization, and Dissolved Oxygen Saturation. A. Mishonov Technical Editor.  
 741 NOAA Atlas NESDIS 83, 38pp, 2019a.

742 Garcia H.E., K.W. Weathers, C.R. Paver, I. Smolyar, T.P. Boyer, R.A. Locarnini, M.M. Zweng, A.V.  
 743 Mishonov, O.K. Baranova, D. Seidov, and J.R. Reagan. World Ocean Atlas 2018. Vol. 4: Dissolved  
 744 Inorganic Nutrients (phosphate, nitrate and nitrate+nitrite, silicate). A. Mishonov Technical Editor,  
 745 NOAA Atlas NESDIS 84, 35pp, 2019b.

746 GEBCO Bathymetric Compilation Group 2021: The GEBCO\_2021 Grid - a continuous terrain model  
 747 of the global oceans and land. NERC EDS British Oceanographic Data Centre NOC.  
 748 doi:10.5285/c6612cbe-50b3-0cff-e053-6c86abc09f8f, 2021.

749 Gelaro, R., McCarty, W., Suárez, M. J., Todling, R., Molod, A., Takacs, L., Randles, C. A.,  
750 Darmenov, A., Bosilovich, M. G., Reichle, R., Wargan, K., Coy, L., Cullather, R., Draper, C., Akella, S.,  
751 Buchard, V., Conaty, A., da Silva, A. M., Gu,  
752 W., Kim, G.-K., Koster, R., Lucchesi, R., Merkova, D., Nielsen, J. E., Partyka, G., Pawson, S.,  
753 Putman, W., Rienecker, M., Schubert, S. D., Sienkiewicz, M., & Zhao, B.: The Modern-Era Retrospective  
754 Analysis for Research and Applications, Version 2 (MERRA-2), *Journal Of Climate*, 30, 5419-5454,  
755 2017.

756 Iselin, C. O. D.: The influence of vertical and lateral turbulence on the characteristics of the waters at  
757 mid-depths, *Eos, Transactions American Geophysical Union*, 20(3). doi 10.1029/TR020i003p00414,  
758 1939.

759 Jain, V., Shankar, D., Vinayachandran, P.N. et al.: Evidence for the existence of Persian Gulf Water  
760 and Red Sea Water in the Bay of Bengal. *Clim Dyn* **48**, 3207–3226. doi: 10.1007/s00382-016-3259-4,  
761 2017

762 Johnson, K. S., J. N. J. N. Plant, S. C. Riser, and D. Gilbert: Air Oxygen Calibration of Oxygen  
763 Optodes on a Profiling Float Array, *Journal of Atmospheric and Oceanic Technology*, 2160–2172. doi  
764 10.1175/JTECH-D-15-0101.1, 2015

765 Karnauskas, K. B., and B. H. Jones: The Interannual Variability of Sea Surface Temperature in the  
766 Red Sea From 35 Years of Satellite and In Situ Observations, *Journal of Geophysical Research: Oceans*,  
767 123(8), 5824-5841, doi: 10.1029/2017JC013320, 2018.

768 Kheireddine, M., Dall'Olmo, G., Ouhssain, M., Krokos, G., Claustre, H., Schmechtig, C., et al.:  
769 Organic carbon export and loss rates in the Red Sea. *Global Biogeochemical Cycles*, 34, e2020GB006650.  
770 doi:[10.1029/2020GB006650](https://doi.org/10.1029/2020GB006650), 2020

771 Krokos, G., Cerovečki, I., Papadopoulos, V. P., Hendershott, M. C., & Hoteit, I.: Processes governing  
772 the seasonal evolution of mixed layers in the Red Sea. *Journal of Geophysical Research: Oceans*, 127,  
773 e2021JC017369. <https://doi.org/10.1029/2021JC017369>, 2022.

774 Kürten, B., Al-Aidaroos, A. M., Kürten, S., El-Sherbiny, M. M., Devassy, R. P., Struck, U., ...  
775 Sommer, U. . Carbon and nitrogen stable isotope ratios of pelagic zooplankton elucidate ecohydrographic

776 features in the oligotrophic Red Sea. *Progress in Oceanography*, 140, 69–90.  
 777 <https://doi.org/10.1016/j.pocean.2015.11.003>, 2016.

778 Kürten, B., Zarokanellos, N. D., Devassy, R. P., El-Sherbiny, M. M., Struck, U., Capone, D. G., et al.  
 779 Seasonal modulation of mesoscale processes alters nutrient availability and plankton communities in the  
 780 Red Sea. *Progress in Oceanography*, 173, 238–255. <https://doi.org/10.1016/j.pocean.2019.02.007>, 2019

781 Lea, D. J., Mirouze, I., Martin, M. J., King, R. R., Hines, A., Walters, D. and Thurlow, M.: Assessing  
 782 a new data assimilation system based on the Met Office coupled atmosphere-land-ocean-sea ice model.  
 783 *Monthly Weather Review*, 143, 4678–4694,. doi 10.1175/MWR-D-15-0174.1, 2015

784 Lozier, M. S.: Evidence for large-scale eddy-driven gyres in the North Atlantic, *Science*, 277(5324),  
 785 361– 364, doi: 10.1126/science.277.5324.361, 1997.

786 Mahadevan A. The Impact of Submesoscale Physics on Primary Productivity of Plankton. *Ann Rev*  
 787 *Mar Sci*. 2016;8:161-84. doi: 10.1146/annurev-marine-010814-015912. 2015

788 Manasrah, R.. The general circulation and water masses characteristics in the Gulf of Aqaba and  
 789 northern Red Sea. Ph.D. thesis, Meereswissenschaftliche Berichte Institut für Ostsee Forschung  
 790 Warnemünde, Universität Rostock, 2002.

791 Manasrah, Mohammad Badran, Hans Ulrich Lass, and Wolfgang Fennel: Circulation and winter deep-  
 792 water formation in the northern Red Sea, *Oceanologica*, 46(1), 5-23, 2004.

793 Morcos: Physical and Chemical Oceanography of the Red Sea, *Annual Review*, 8, 73-202. doi:  
 794 10.12691/ajwr-3-3-2

795 Mohamed B. and Skliris N., Recent sea level changes in the Red Sea: Thermosteric and halosteric  
 796 contributions, and impacts of natural climate variability. *Progress in Oceanography*, Vol 231, 103416,  
 797 <https://doi.org/10.1016/j.pocean.2025.103416>, 2025.

798 Morcos, and Soliman (1972), Circulation and deep water formation in the northern Red Sea in winter,  
 799 *L'Océanographie Physique de la Mer Rouge*, UNESCO, 91–103, 1970

800 Adele K. Morrison, Darryn W. Waugh, Andrew McC. Hogg, Daniel C. Jones, Ryan P. Abernathey:  
 801 Ventilation of the Southern Ocean Pycnocline, *Annual Review of Marine Science* 14:1, 405-430, 2022.

802 Murray, S. P., and W. Johns: Direct observations of Bab el Mandab Strait, *Geophysical Research*  
 803 *Letters* 24(21), 2557-2560. doi: 10.1029/97GL02741, 1997.

804 OBPG, MODIS Aqua Level 3 SST Thermal IR Daily 4km Daytime v2014.0. Ver. 2014.0.  
805 PO.DAAC, CA, USA. Dataset accessed at [doi: 10.5067/MODSA-1D4D4](https://doi.org/10.5067/MODSA-1D4D4), 2015.

806 Papadopoulos, V. P., Y. Abualnaja, S. A. Josey, A. Bower, D. E. Raitsos, H. Kontoyiannis, and I.  
807 Hoteit : Atmospheric forcing of the winter air-sea heat fluxes over the northern Red Sea, *Journal of*  
808 *Climate*, 26, 1685–1701. doi: 10.1175/JCLI-D-12-00267.1, 2013

809 Papadopoulos, V. P., et al.: Factors governing the deep ventilation of the Red Sea, *Journal of*  
810 *Geophysical Research: Oceans*, 120(11), 7493-7505, doi:10.1002/2015JC010996, 2015.

811 Patzert, W.: Wind-induced reversal in Red Sea circulation, *Deep-Sea Research*, 21, 109-121.doi:  
812 10.1016/0011-7471(74)90068-0, 1974.

813 Price, J., R. Weller, and R. Pinkel: Diurnal Cycling' Observations and Models of the Upper Ocean  
814 Response to Diurnal Heating, Cooling, and Wind Mixing *Journal of Geophysical Research*, 91(C7), 8411-  
815 8427. doi: 10.1029/JC091iC07p08411, 1986

816 Quadfasel, D., and H. Baudner: Gyre-scale circulation cells in the Red Sea, *Oceanologica Acta*, 16(3),  
817 221-229, 1993.

818 Raitsos, D. E., Y. Pradhan, R. J. W. Brewin, G. Stenchikov, and H. I.: Remote sensing the  
819 phytoplankton seasonal succession of the Red Sea, *PLoS ONE*, 8(6), e64909.  
820 doi:10.1371/journal.pone.0064909, 2013.

821 Rienecker, M. M., et al.: MERRA: NASA's Modern-Era Retrospective Analysis for Research and  
822 Applications, *Journal of Climate*, 24(14), 3624-3648, doi:10.1175/JCLI-D-11-00015.1, 2011.

823 Roesler, C., Uitz, J., Claustre, H., Boss, E., Xing, X., Organelli, E., Briggs, N., Bricaud, A.,  
824 Schmechtig, C., Poteau, A., D'Ortenzio, F., Ras, J., Drapeau, S., Haëntjens, N., & Barbieux, M:  
825 Recommendations for obtaining unbiased chlorophyll estimates from in situ chlorophyll fluorometers: A  
826 global analysis of WET Labs ECO sensors, *Limnology and Oceanography Methods* 15(6), 572-585.doi:  
827 10.1002/lom3.10185, .2017.

828 Sanikommu, S., Toye, H., Zhan, P., Langodan, S., Krokos, G., Knio, O., &Hoteit, I. Impact of  
829 atmospheric and model physics perturbations on a high-resolution ensemble data assimilation system of  
830 the Red Sea. *Journal of Geophysical Research: Oceans*, 125, e2019JC015611.  
831 <https://doi.org/10.1029/2019JC015611>, 2020.

832 Schott, F. A., and J. P. McCreary: The monsoon circulation of the Indian Ocean, *Progress in*  
833 *Oceanography*, 51(1), 1-123, doi:10.1016/S0079-6611(01)00083-0, 2001.

834 Smeed, D.: Seasonal variation of the flow in the strait of Bab al Mandab, *Oceanologica Acta*, 20(6),  
835 773-781, 1997.

836 Sofianos, S., and W. Johns: An Oceanic General Circulation Model (OGCM) investigation of the Red  
837 Sea circulation, 1. Exchange between the Red Sea and the Indian Ocean, *Journal of Geophysical Research*  
838 107(C11), 3196, doi:10.1029/2001JC001184, 2002.

839 Sofianos, S. and W. E. Johns: An Oceanic General Circulation Model (OGCM) investigation of the  
840 Red Sea circulation: 2. Three-dimensional circulation in the Red Sea, *Journal of Geophysical Research*,  
841 108(C3), 1-15, doi:10.1029/2001JC001185, 2003.

842 Sofianos, S. and W. E. Johns: Observations of the summer Red Sea circulation, *Journal of*  
843 *Geophysical Research*, 112(C06025), 1-20, doi:10.1029/2006JC003886, 2007.

844 Sofianos, S. S., W. E. Johns, and S. P. Murray: Heat and freshwater budgets in the Red Sea from  
845 direct observations at Bab el Mandeb, *Deep-Sea Research Part II-Topical Studies in Oceanography*, 49(7-  
846 8), 1323-1340, doi:10.1016/S0967-0645(01)00164-3, 2002

847 TEOS, SCOR, and IAPSO: The international thermodynamic equation of seawater – 2010:  
848 Calculation and use of thermodynamic properties, Intergovernmental Oceanographic Commission,  
849 UNESCO, Paris, 196 pp, 2010.

850 Triantafyllou, G., F. Yao, G. Petihakis, K. P. Tsiaras, D. E. Raitsos, and I. Hoteit, Exploring the Red  
851 Sea seasonal ecosystem functioning using a three-dimensional biophysical model, *Journal of Geophysical*  
852 *Research-Oceans*, 119(3), 1791-1811, doi:10.1002/2013jc009641, 2014.

853 Werdell, P. J., et al.: Generalized Ocean color inversion model for retrieving marine inherent optical  
854 properties, *Appl Optics*, 52(10), 2019-2037, doi:10.1364/Ao.52.002019, 2013.

855 Williams R.G., Meijers A.: Ocean subduction, Cochran J.K., Bokuniewicz H.J., Yager P.L. (Eds.),  
856 *Encyclopedia of Ocean Sciences* (3rd ed.), Academic Press, Cambridge, Massachusetts, United States,  
857 pp. 141-157, [10.1016/B978-0-12-409548-9.11297-7](https://doi.org/10.1016/B978-0-12-409548-9.11297-7), 2019

858 Woelk, S., and D. Quadfasel: Renewal of deep water in the Red Sea during 1982-1987, *Journal of*  
859 *Geophysical Research-Oceans*, 101(C8), 18155-18165, doi:10.1029/96jc01148, 1996.

860 Yao, F., and I. Hoteit (2018), Rapid Red Sea Deep Water renewals caused by volcanic eruptions and  
861 the North Atlantic Oscillation, *Science Advances* 4(6), doi:10.1126/sciadv.aar5637.

862 Yao, F., I. Hoteit, L. J. Pratt, A. S. Bower, P. Zhai, A. Köhl, G. Gopalakrishnan: Seasonal overturning  
863 circulation in the Red Sea: 1. Model validation and summer circulation, *J. Geophys. Res. Oceans*, 119,  
864 doi:10.1002/2013JC009004, 2014a.

865 Yao, F., I. Hoteit, L. J. Pratt, A. S. Bower, A. Köhl, G. Gopalakrishnan, and D. Rivas : Seasonal  
866 overturning circulation in the Red Sea: 2. Winter circulation, *J. Geophys. Res. Oceans*, 119, 2263–2289,  
867 doi:10.1002/2013JC009331, 2014b.

868 Zarokanellos, N. D., B. Kürten, J. H. Churchill, C. Roder, C. R. Voolstra, Y. Abualnaja, and B. H.  
869 Jones: Physical Mechanisms Routing Nutrients in the Central Red Sea, *Journal of Geophysical Research:*  
870 *Oceans*, 122, doi:10.1002/2017JC013017, 2017a.

871 Zarokanellos, N. D., V. P. Papadopoulos, S. S. Sofianos, and B. H. Jones: Physical and biological  
872 characteristics of the winter-summer transition in the Central Red Sea, *Journal of Geophysical Research-*  
873 *Oceans*, 122(8), 6355-6370, doi:10.1002/2017jc012882, 2017b.

874 Zarokanellos, N., and B. H. Jones: Winter mixing, mesoscale eddies and eastern boundary current:  
875 Engines for biogeochemical variability of the central Red Sea during winter/early spring period., *Journal*  
876 *of Geophysical Research-Oceans*, accepted, doi:10.1029/2020JC016714, 2021.

877 Zarokanellos, N. D., Rudnick, D. L., Garcia-Jove, M., Murre, B., Ruiz, S., Pascual, A., & Tintoré,  
878 J.. Frontal dynamics in the Alboran Sea: 1. Coherent 3D pathways at the Almeria-Oran front using  
879 underwater glider observations. *Journal of Geophysical Research: Oceans*, 127, e2021JC017405.  
880 <https://doi.org/10.1029/2021JC017405>, 2022.

881 Zhai, P., A. S. Bower, W. M. S. Jr., and L. J. Pratt: Formation and spreading of Red Sea Outflow  
882 Water in the Red Sea, *Journal of Geophysical Research*, 120(9), 6542-6563, doi:10.1002/2015JC010751,  
883 2015.

884 Zhan, P., G. Gopalakrishnan, A. C. Subramanian, D. Guo, and I. Hoteit: Sensitivity Studies of the  
885 Red Sea Eddies Using Adjoint Method, *Journal of Geophysical Research: Oceans*, 123,  
886 doi:10.1029/2018JC014531, 2018.

887 Zhan, P., G. Krokos, D. Q. Guo, and B. Hoteit: Three-Dimensional Signature of the Red Sea Eddies



888 and Eddy-Induced Transport, *Geophysical Research Letters*, 46(4), 2167-2177,  
889 doi:10.1029/2018gl081387, 2019.

890 Zhan, P., A. C. Subramanian, F. Yao, and I. Hoteit: Eddies in the Red Sea: A statistical and dynamical  
891 study, *Journal of Geophysical Research: Oceans*, 119(6), 3909-3925, doi:10.1002/2013JC009563, 2014.

892 Zhan, P., A. C. Subramanian, F. Yao, A. R. Kartadikaria, D. Guo, and I. Hoteit: The eddy kinetic  
893 energy budget in the Red Sea, *Journal of Geophysical Research*, 121(7), 4732-4747, doi:  
894 10.1002/2015JC011589, 2016.

895 Zhang, Z., and J. C. Moore: *Mathematical and Physical Fundamentals of Climate Change*, Elsevier,  
896 doi: 10.1016/B978-0-12-800066-3.00006-1, 2015.